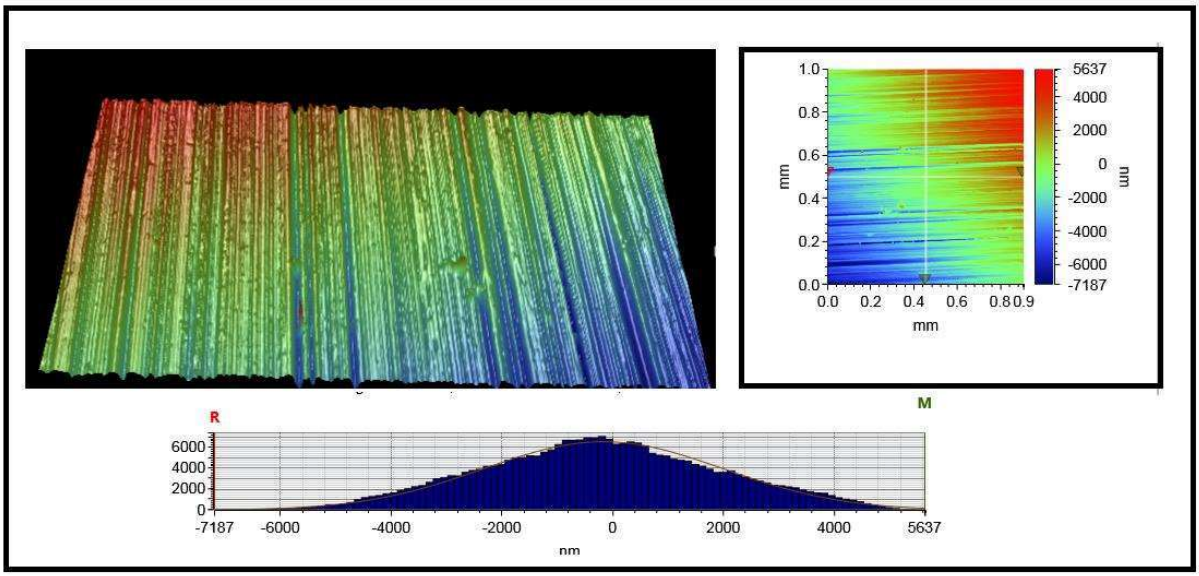
RESULTS AND DISCUSSION

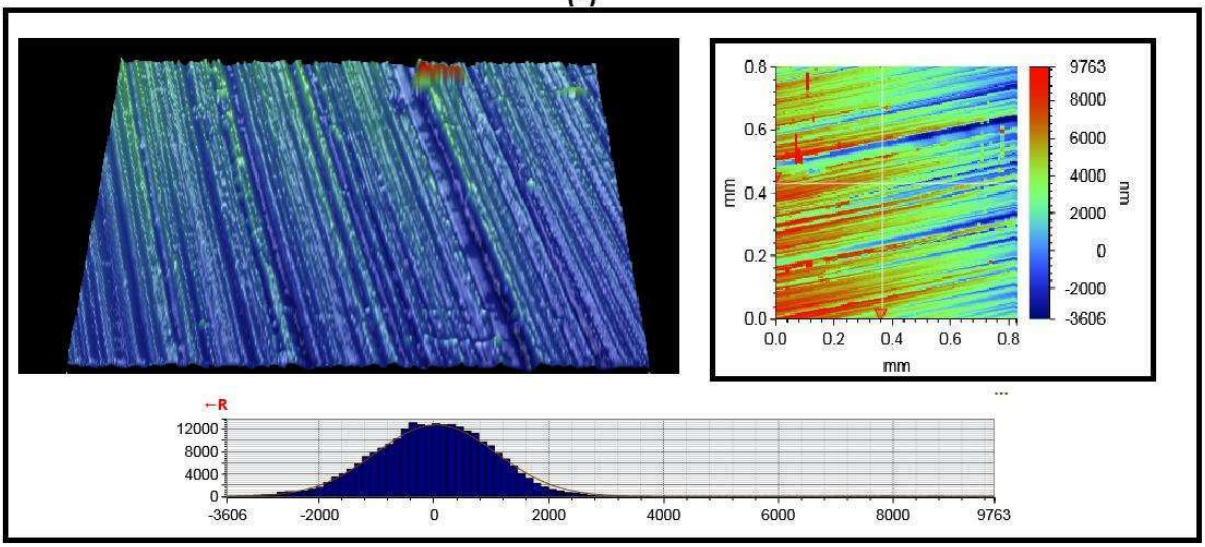
5.1 MATERIAL SELECTION AND CHARACTERIZATION

5.1 .1 Surface Roughness Measurement

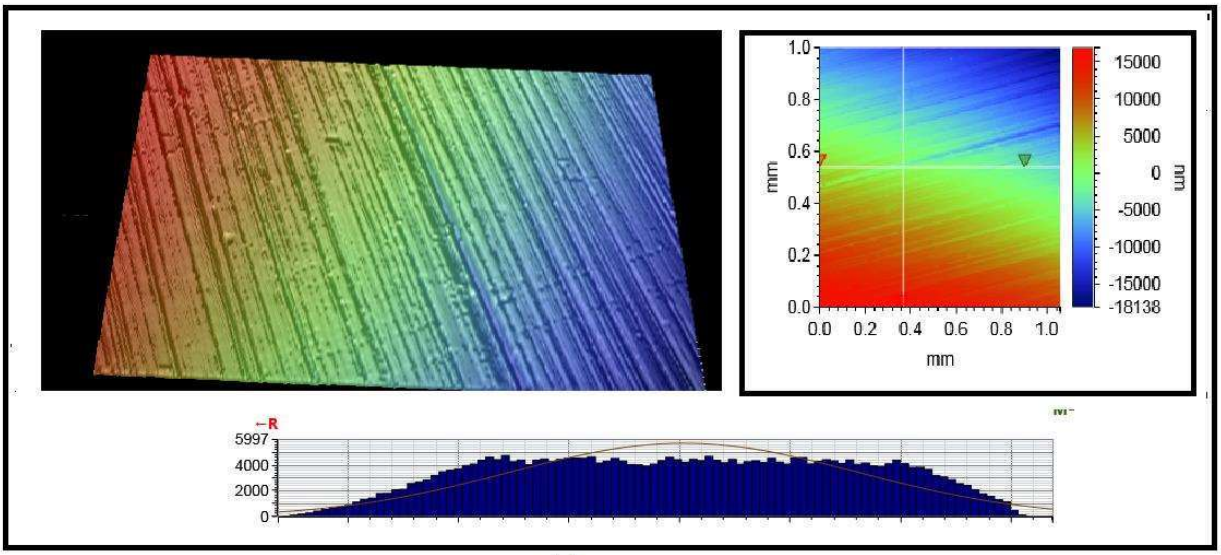
The surface morphology of the metal specimen achieved with different levels of polishing, using different grades of emery polishing paper are shown in Figure 5.1(a-c).



(a)



(b)



(c)

Figure 5.1: Surface morphology of metal specimens: (a) as received condition, (b) low level (c) and high level of surface roughness

The surface roughness values of all metal specimens increased as emery paper grade size decreases (Figure 5.2).

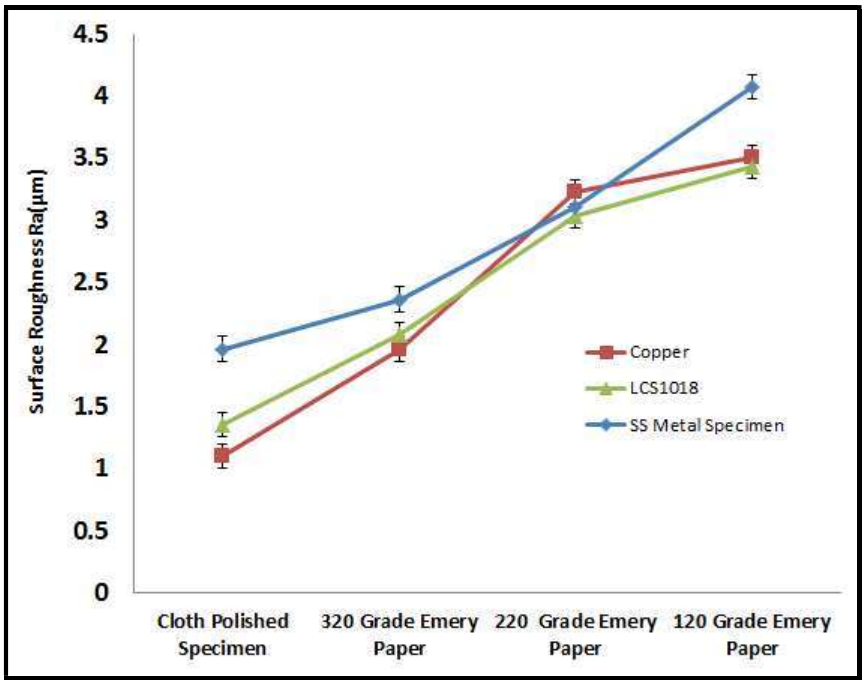


Figure 5.2: Surface roughness variation with different grade emery paper

5.1.2 Results of Pre-oxidation Study

In case of SS304 after pre-oxdizing at 700 ˚C for 3 minutes, the oxide layer mass gain (g/cm^2) obtained on the specimen, increased with increase in surface roughness value of the substrate. The oxide layer mass gain in case of SS304 specimen increased in range (0.3×10^{-4}-0.8×10^{-4})g/cm^2 as shown in Figure 5.3. The oxide layer thickness was also increased from (63.78 to 81.68 µm) as shown in Figure 5.3.

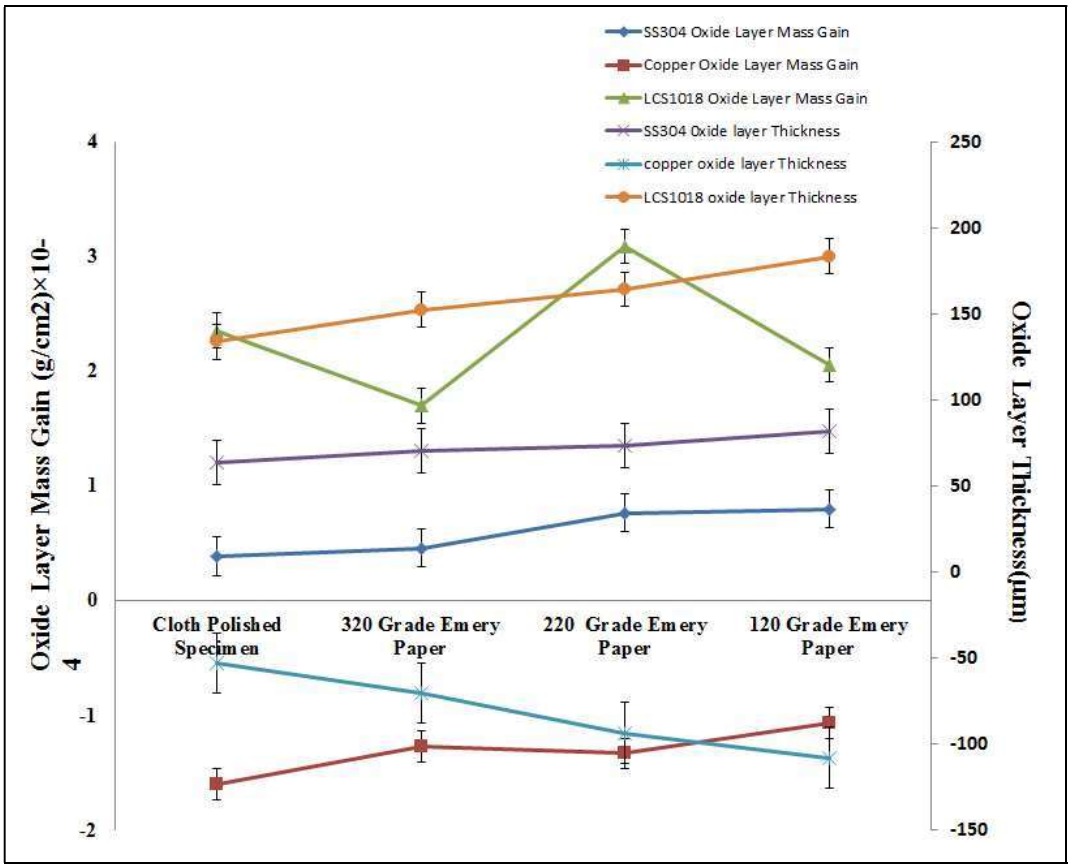


Figure 5.3: Oxide mass gain of different metal specimen at 700°C for 3 minutes

The micrograph of oxide layer thickness shows that as surface roughness values of metal specimen increase the increased oxide deposition was observed in the waviness region of the metal specimen as shown in Figure 5.4(a-d).

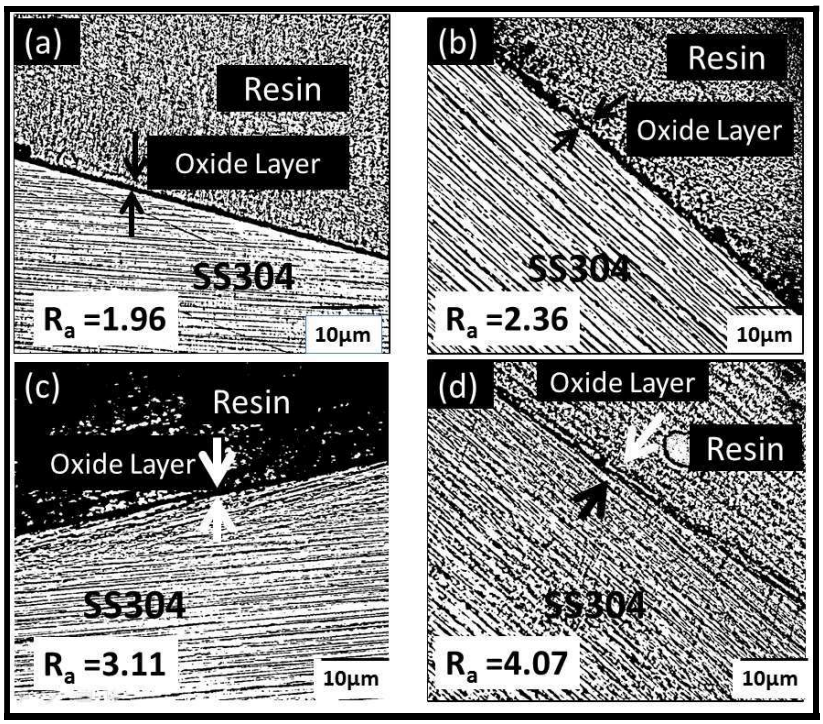


Figure 5.4(a-d): The oxide layer thicknesses on SS304 metal specimen with increasing surface roughness R_a (1.96-4.07µm)

The oxide layer thickness formed on the surface of the SS304 metal specimen after the pre-oxidation also increased with the increase in surface roughness increased. The micrograph of oxide layer formed on the surface of metal specimens is as shown in Figure.5.4 (a-d).
In case of copper, the oxide layer mass gain was observed to be a negative value as shown in (Figure 5.3). The oxide layer increased with increase in the surface roughness of copper increased and this is due to the increased waviness of metal specimen at the elevated temperature as shown in Figure 5.5 (a-d).

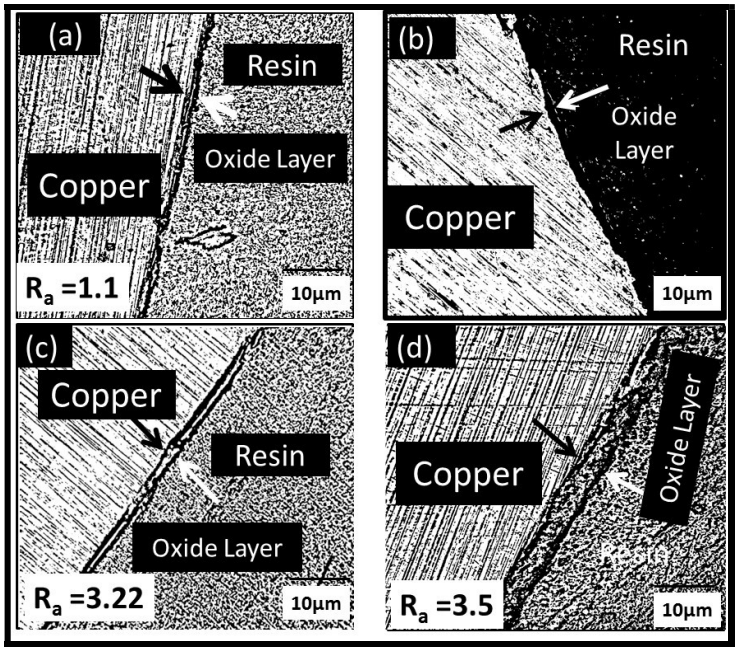


Figure 5.5 (a-d): The oxide layer thickness of copper metal specimen with increasing surface roughness R_a(1.1-3.5µm)

The top layer of oxidized copper substrate detached from the surface of copper during pre-oxidation at 700°C as shown in Figure 5.13(e). This leads to the reduction of oxide layer mass gain in the range -(1.59 to 1.06×10^{-4}) g/cm^2 (negative) as shown in Figure 5.3.

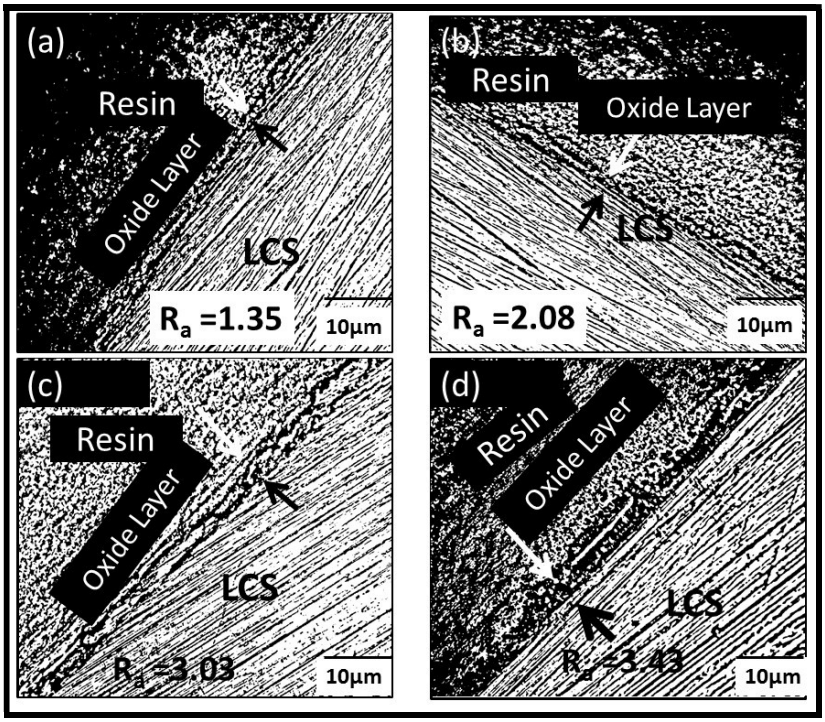


Figure 5.6 (a-d): Oxide layer thickness in LCS 1018 metal specimen after pre-oxidation at 700°C at different surface roughness R_a(1.35-3.43µm)

The micrograph of copper used to examine the oxide layer thickness is as shown in Figure 5.5(a-d). The maximum oxide layer thickness corresponding to maximum surface roughness is shown in Figure 5.5 (d).The oxide layer thickness in the case of LCS1018 is higher than SS304 and copper specimen. The oxide layer thickness of LCS 1018 metal specimen was found to increase with the increase in surface roughness of metal from (133.75 to 183.77µm) as depicted in Figure 5.3. The micrographs of LCS1018 metal specimen after pre-oxidation at 700^{0}C for 3 minutes with different surface roughness is Figure 5.6(a-d).

5.1.3 Nature of Oxide formation

The types of oxide formed in the SS304 metal specimen during the different stages of glass-metal joint fabrication are shown in Figure 5.7. The fresh (as received) SS304 metal specimen consists of chromium, iron, nickel, and carbon (Fe $Cr_{0.29}$ Ni $_{0.16}$ $C_{0.06}$). As metal pre-oxidized at 700°C, FeO (iron oxide) having closed cubic configuration is formed which confirmed the pre-oxidation of the metal specimen as shown in the XRD pattern in Figure 5.7.

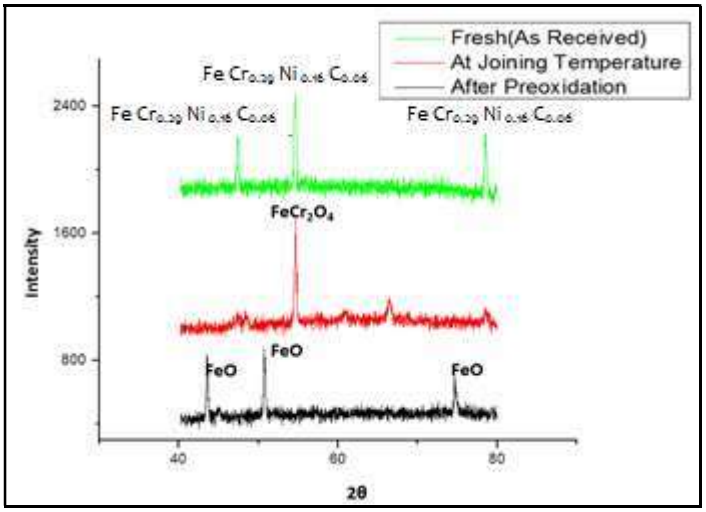


Figure 5.7 XRD: pattern of SS 304 in as-received, in pre-oxidation and in joining condition

As temperature of metal specimen reaches to joining temperatures at 980 ˚C no carbon phase was observed as shown in Figure 5.7. The formation of an inorganic component iron chromite phase was observed as shown in the XRD pattern of SS304 at joining temperature. Above 700 ˚C pre-oxidation temperature the precipitation of carbon in form of carbide from the grain boundary of metal takes place.

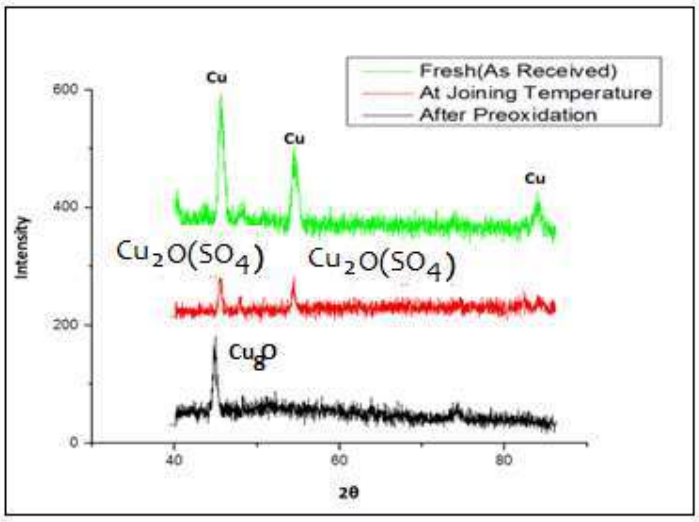


Figure 5.8: XRD pattern of copper in as-received, in pre-oxidation and in joining condition

From the XRD analysis, the fresh copper (as received) is shown in Figure 5.8 consists of pure copper (Cu). As metal gets pre-oxidized at 700 ˚C, Cu_8O and $Cu_2O(SO_4)$ phases were obtained which shows that metal has been pre-oxidized. The Cu_8O oxide phase has been reported as more exotic metastable compound formed on the copper during the initial stage of copper pre-oxidation. At the joining condition crystal of dolerphanite phase $Cu_2O(SO_4)$ was observed having 66.52% CuO and 33.48% SO_3 [Guan.R et.al.1984]. The XRD phase of copper in fresh (as received), pre-oxidized and during joining temperature 980˚C is shown in Figure 5.8.

The fresh LCS (as received) consists of Fe_9O_4 phase. As metal specimen was pre-oxidized at 700 °C, the $Fe_{94}CO_6$ phase was observed as shown in the XRD pattern of LCS1018 which is depicted through Figure 5.9. During the wetting process of glass pallet over LCS1018 specimen, the top layer of metal gets detached from the specimen's top surface and gets fused with glass during melting as shown in Figure.5.13(f). The type of oxide phase obtained in different metals during the different stages of glass-metal joining are summarize in Table 5.1.

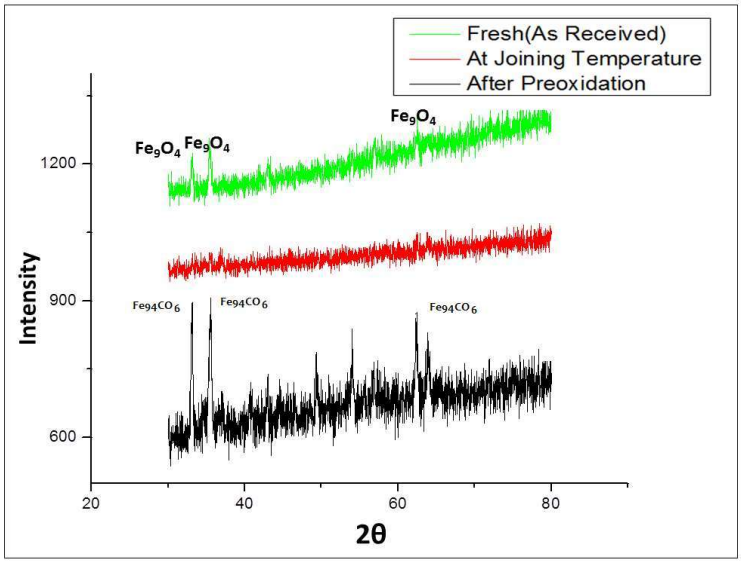


Figure 5.9: XRD pattern of LCS1018 in as-received, in pre-oxidation and in joining condition

Table 5.1: Oxide formed during pre-oxidation process in different metal specimen

Specimen Condition	Austenitic Stainless Steel SS304	Copper	Low carbon Steel LCS1018
As-received Specimen	Fe $Cr_{0.29}$ $Ni_{0.16}$ $C_{0.06}$	Cu	Fe_9O_4
Pre-oxidation 700°C for 3 min.	FeO	Cu_8O	$Fe_{94}CO_6$
At Joining Condition 980°C	$FeCr_2O_4$	$Cu_2O(SO_4)$	-

5.1.4 Wettability Study

The contact angle and spreading behavior of borosilicate glass increased with the increase in the surface roughness of metal specimen. The contact angle of glass over SS304 metal specimen increased from 26.19-33.42˚ (Figure 5.10), and it was lower than 45˚ and confirms the good wettability of glass with metal.

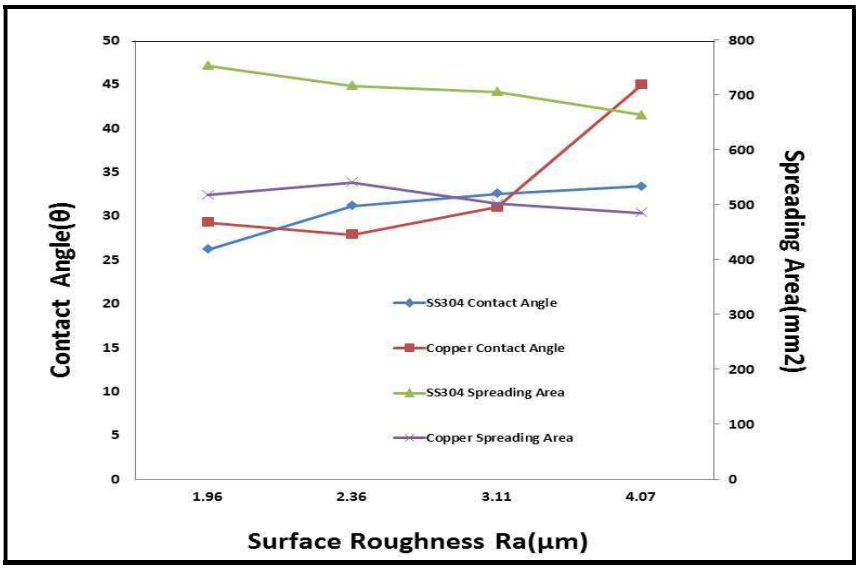


Figure 5.10: Contact angle and wetting area variation with surface roughness of SS304 and copper

The spreading area of glass pallet decreased (754.385-664.748 mm^2) with the increase in the surface roughness Ra value of SS metal specimen (1.96-4.77 μm). The increase in surface roughness of metal specimen decreases the wetting and spreading of glass over the metal specimen because of the waviness surface generated on the surface metal. The waviness in the surface of metal increases the value of contact angle and the higher value of contact angle decreases the wettability as the surface roughness increases.
The wettability of borosilicate glass over metal specimen was observed to be a maximum in case of austenitic stainless steel SS304, therefore, SS304 was considered as suitable metal for the fabrication of unmatched glass metal joint.

5.2 DEVELOPMENT OF UNMATCHED GLASS-METAL JOINT

The unmatched glass-metal joint was fabricated by taking the SS304 metal ring and borosilicate glass tube and space between the metal ring and borosilicate glass tube was filled with glass sealant. The fabricated glass-metal joint is shown in Figure 5.11(a-b). The cracking of glass tube at the inner side of the metal ring was observed after the fabrication of joint which occurred, because of higher metal ring thickness and higher intensity of residual stress.

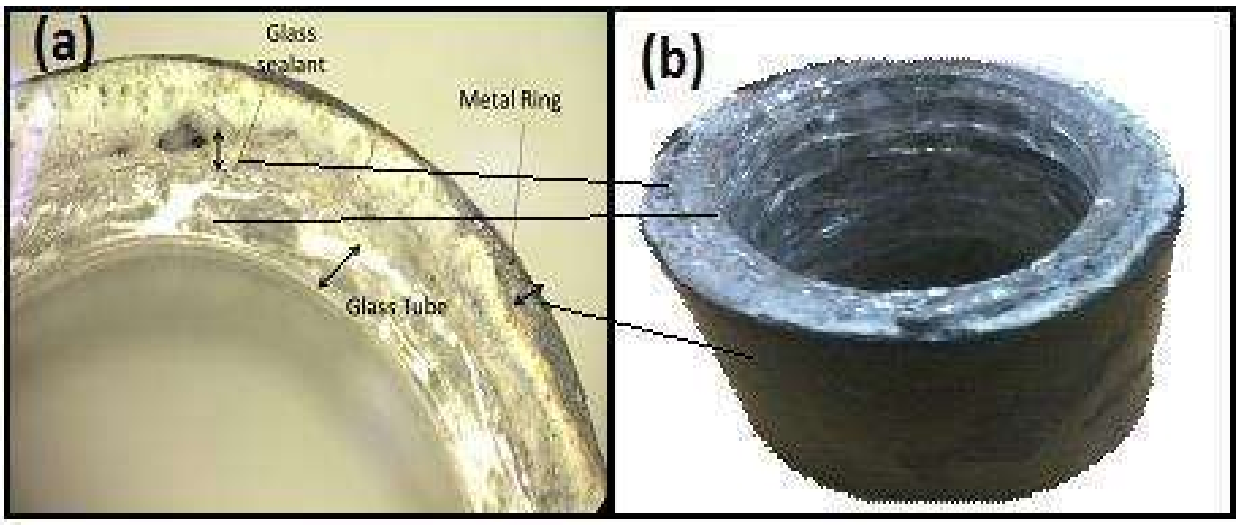


Figure 5.11: (a) The top view of glass-metal joint interface,(b) Front view of failed compression glass-metal joint

5.2.1 Residual Stress Measurement

In order to understand the cracking phenomenon of glass tube after the fabrication of compression glass-metal joint, residual stress measurement was carried out in the glass tube by reducing the thickness of metal ring using the photo-elastic technique.

The glass-metal joint assembly after fabrication was placed between polarizer and analyzer as shown in Figure 5.12(a). The residual stresses develop in the glass tube were observed to be in the form of gray and black intensity as shown in Figure 5.12(b). The tint plate was then installed between polarizer and analyzer above the glass-metal in order to see the intensity of stresses in glass tube after the fabrication of glass-metal joint and the stresses in glass tube were observed corresponding to 2 mm and 0.4 mm metal ring thickness as shown in Figure 5.12(c and d respectively).

The result obtained with polarimeter indicates that as the thickness of metal ring increases the intensity of tensile stresses developed in glass tube also increases causing the breaking of glass tube just few millimeters above the interface. The tensile residual stresses developed in glass tube after fabrication corresponding to 2.5mm metal thickness were measured around 350(MPa) which is higher that ultimate tensile strength of borosilicate glass tube of 280 (MPa).

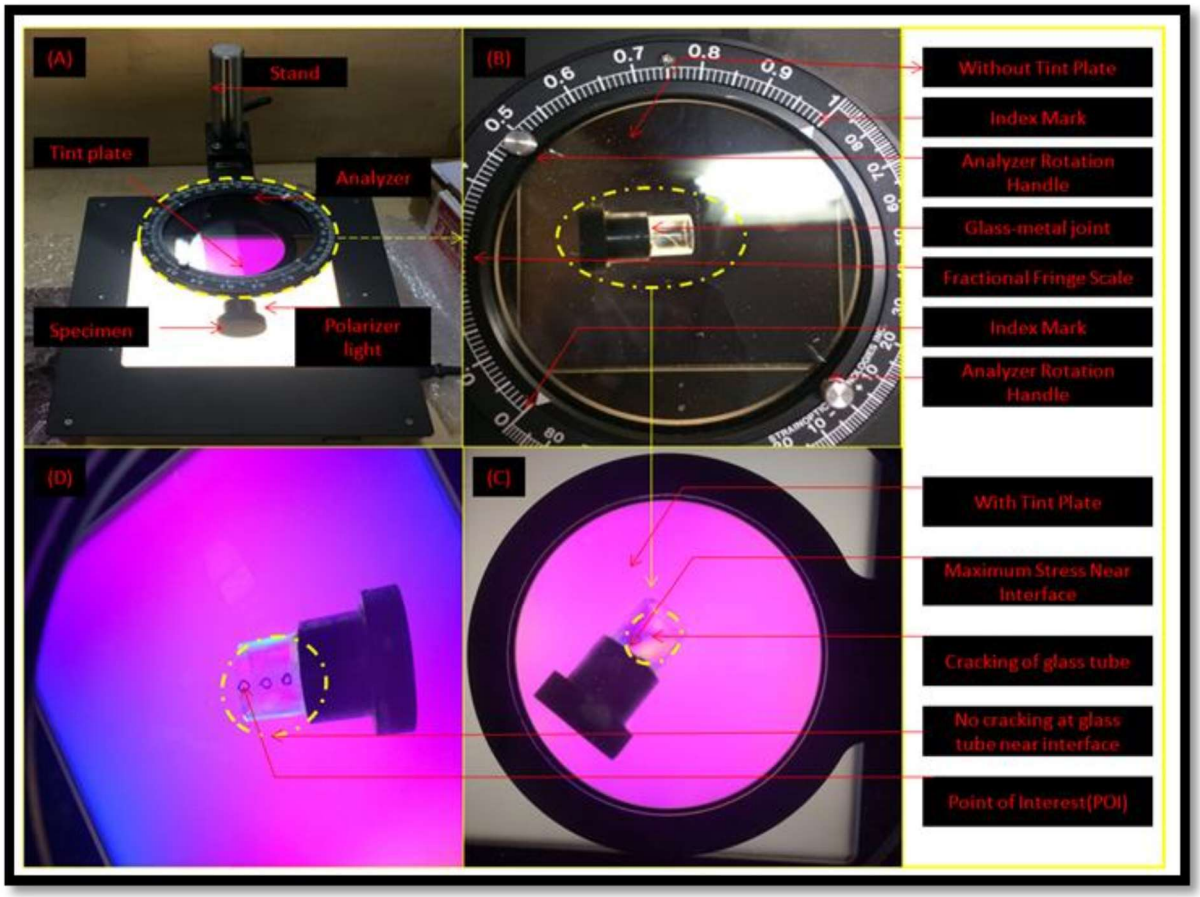


Figure 5.12: (a) Polariscope "PS-100-BS" set-up **(b)** Stress calculation without tint plate.**(c)** Stress calculation with tint plate corresponding to 2mm metal thickness**(d)** Stress calculation with tint plate corresponding to 0.4 mm metal thickness

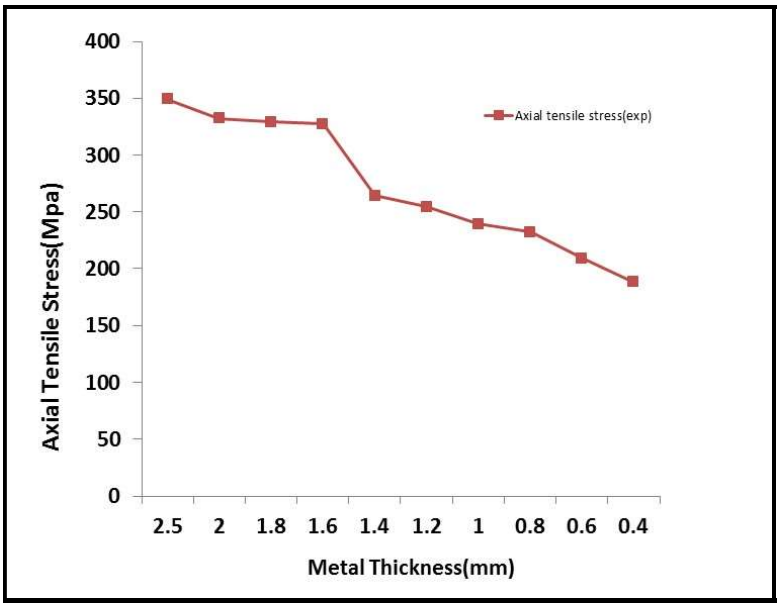


Figure 5.13: Residual axial stress variations with respect to metal thickness

The high value of measured tensile stress breaks the glass tube at the interface of glass-metal joint as shown in Figure 5.14.

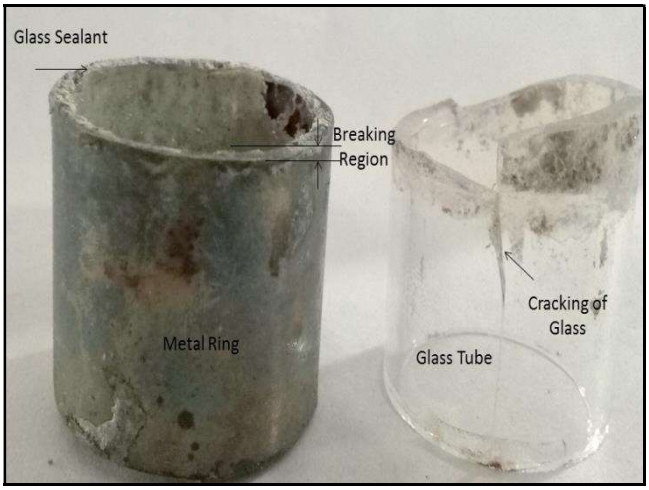
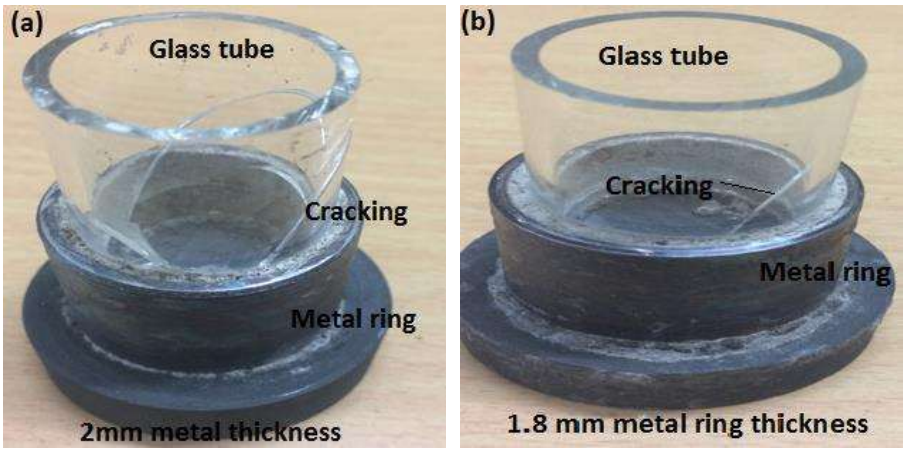


Figure 5.14: Cracking of glass tube because of the higher metal ring thickness (2.5mm)

As the thickness of metal ring reduces from 2.5 to 2 mm the cracking of glass tube was observed near the interface as shown in Figure 5.15 (a). As the thickness of metal ring further reduces from 2.5 mm to 1.6 mm, the value of tensile stress was obtained in between (300-350 MPa) which is higher than ultimate tensile strength of glass.



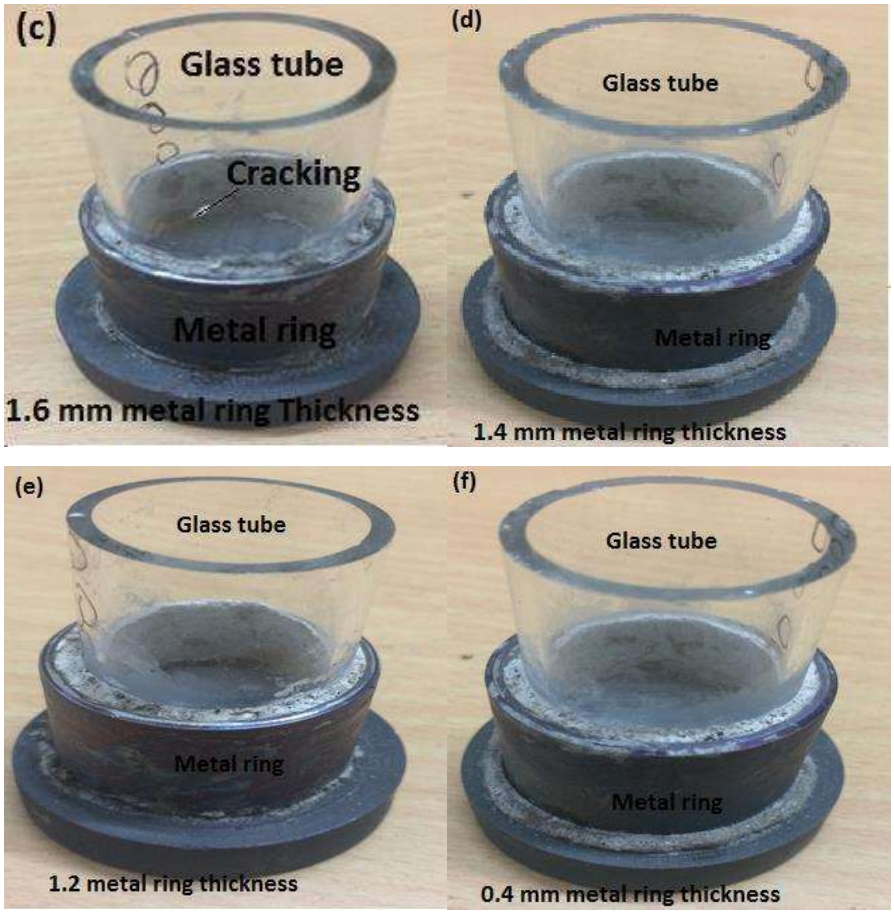


Figure 5.15 (a-f): Failure Condition of glass-metal joint assembly after fabrication with decrease in metal thickness

The cracking in the glass tube is observed up to 1.6 mm thickness as shown in Figure.5.15(a-c) As the metal thickness further decreases from 1.6 mm to 0.4 mm the tensile stress value also decreased from (265-189 MPa), which is lower than the ultimate tensile strength of glass tube. Therefore, the quality of joint was improved in terms of cracking resistance as the thickness of metal ring decreased from 1.6 mm to 0.4 mm as shown in Figure 5.15 (d-f). The residual axial stress variations with respect to metal thicknesses shown in Figure.5.13

The progressive failure of compression glass-metal joint with variation in metal thickness after fabrication of joint is shown in Figure 5.15 (a-f). The failure of joint occurs corresponding to 2.5 mm, 2mm, 1.8 mm, 1.6 mm values of metal thickness as shown in Figure 5.14 and Figure 5.15 (a-c) respectively. As the thickness of metal ring reduces, the cracking of joint was eliminated as shown in Figure 5.15 (d-f), leading to the enhancement in quality of joints in terms of crack-free joint.

5.2.2 Thermal Expansion Mismatch

The magnitude of stress induced in glass-metal joint also depends upon the difference in coefficient of thermal expansion mismatch.

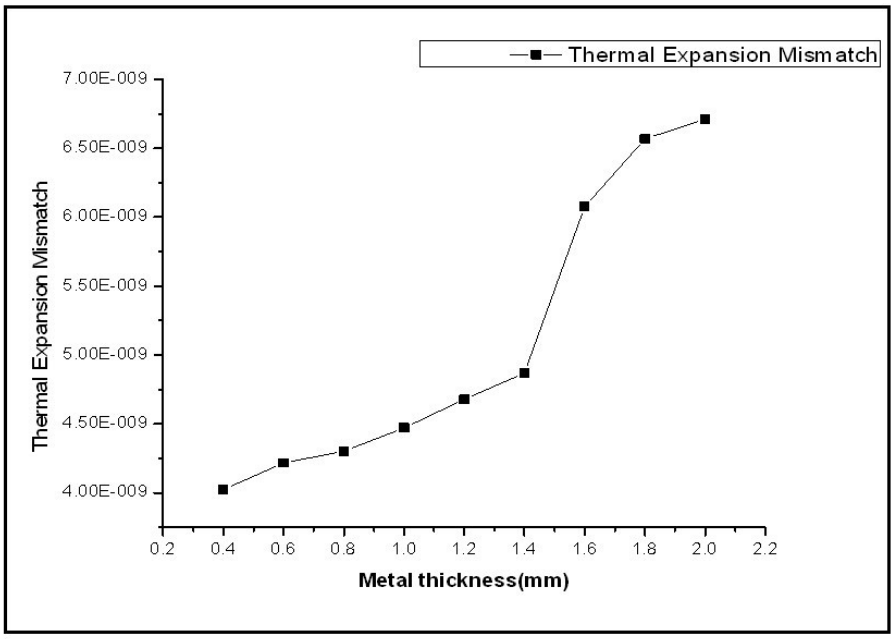


Figure 5.16: Variation of Thermal expansion mismatch with different metal thicknesses

The thermal expansion mismatch between the glass-metal joint also increases with increasing the thickness of metal ring as shown in Figure 5.16.

From the experimental result of tensile residual stress and thermal expansion mismatch, it has been proved that intensity of stress depends directly upon the thermal expansion mismatch.

The 0.4 mm metal thickness was considered to be an adequate thickness where lower value of residual stresses and thermal expansion mismatch was observed. The quality of joint was observed to free from crack the at 0.4 mm metal ring thickness.

5.3 EFFECT OF SiO_2 / B_2O_3 RATIO ON THE PROPERTIES OF GLASS SEALANT

5.3.1 Effect of SiO_2 / B_2O_3 Ratio on Wettability of Glass Sealant

After obtaining the geometry of unmatched glass-metal joint, by taking 0.4 mm metal ring thickness, the development of glass sealant was carried out by changing the SiO_2/B_2O_3 Ratio. The SiO_2/B_2O_3 ratio of glass sealant was tailored by increasing B_2O_3 content and decreasing SiO_2 while keeping percentage of Al_2O_3 and Na_2O constant. The melting of different glass sealant was performed in batch. The spreading behavior of different glass sealants over SS304 is shown in Figure 5.17.

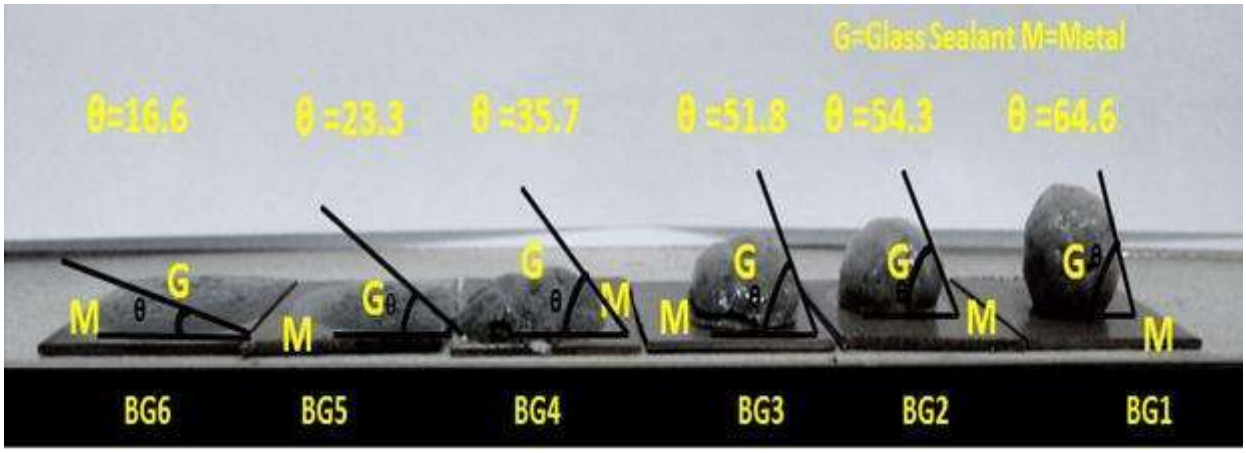


Figure 5.17: Melting and wetting of different glass sealants

The contact angle formed by glass sealant over SS304 metal decreases as SiO_2/B_2O_3 Ratio decreases. The decrease in contact angle by decreasing SiO_2/B_2O_3 Ratio confirms the increase in

wettability of glass sealant over the metal specimen. The spreading behavior of glass sealant increased as SiO_2/B_2O_3 Ratio decreases. The spreading behavior of BG6 glass sealant was observed to be maximum, where the lowest value of SiO_2/B_2O_3 Ratio was obtained. The higher spreading of BG6 glass sealant was obtained because of the higher percentage of B_2O_3 as compare to SiO_2.The adhesion of glass sealants with SS304 metal specimen corresponding to different SiO_2/B_2O_3 Ratio is as shown in Figure 5.18. The adhesion of glass sealant increases as SiO_2/B_2O_3 Ratio decreases which is because of the lower value of contact angle and higher spreading of glass sealant over the metal specimen.

5.3.2 Effect of SIO_2 / B_2O_3 Ratio on Adhesion Strength and Spreading Area of Glass Sealant

The variation of adhesion strength with respect to contact angle formed by glass sealant over the metal specimen is shown in Figure 5.18. The adhesion of glass sealant with SS304 metal specimen increased as contact angle decreased. The lower value of contact angle ensures high wettability and higher spreading as shown in Figure 5.19.

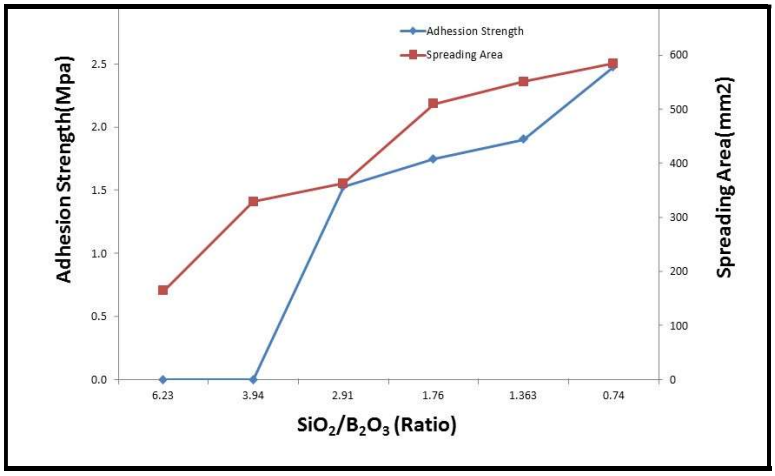


Figure 5.18: Adhesion strength and spreading area variation with different SiO_2/B_2O_3 (Ratio)

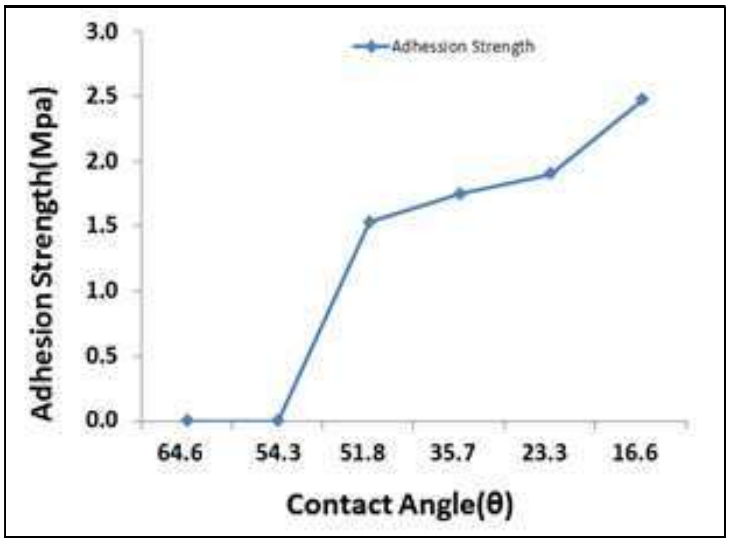


Figure 5.19: Adhesion strength variations with respect to contact angle

5.3.3 Effect of SIO_2 / B_2O_3 Ratio on X-Ray Diffraction Pattern of Glass Sealant

The X-rays pattern of different glass sealant is as shown in Figure 5.20. The absence of sharp peaks in difference glass sealants confirms amorphous nature of glass sealants

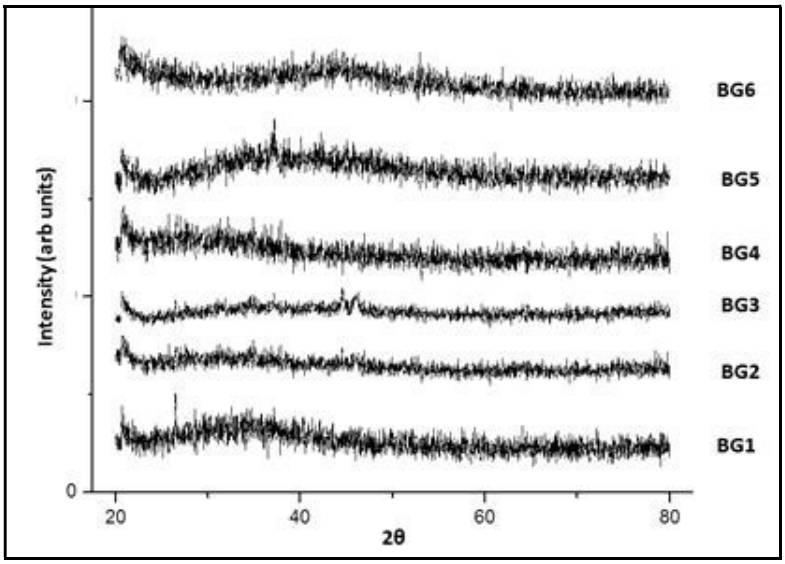


Figure 5.20: XRD pattern of different glass sealant

.

5.3.4 Effect of SiO_2 / B_2O_3 Ratio on Fourier Transform Infrared Spectroscopy (FTIR) of glass sealant

The FTIR spectra of different glass sealants having different SiO_2/B_2O_3 Ratio is as shown in Figure 5.21.

Table 5.2: Assignment of different band observed in the spectra of different glass reported by researchers [Rada.et.al 2006]

S.no	Band observed range (cm^{-1})	Assigned Vibration
1	425-490	SiO_4 tetrahedral formation
2	690-800	Si-O-Si antisymmetric stretching vibration of Si–O–Si in [SiO4] tetrahedral
3	800-1050	BO_4 vibration of tetrahedral (penta, di and triborates)
4	1400-1420	BO_3 unit with non-bridging oxygen
5	1434	BO_3 unit with non-bridging oxygen
6	1380,1250	B-O stretching vibration of trigonal BO_3^- unit in meta borate, pyro borate, and ortho borates
7	880,970,1025, 698	BO_4 vibration of tetrahedral(penta,di and triborates)
8	475-425	Bending of B-O-B linkage of B-O network

The total five peaks were observed in the infrared spectra of each glass sealant in the range shown in Table 5.2. The region between (475- 500 cm^{-1}) ascribed the asymmetric bending vibration of Si-O-Si. Bending vibration of [BO_3] was observed in the range (600-695 cm^{-1}) shown in Table 5.2.

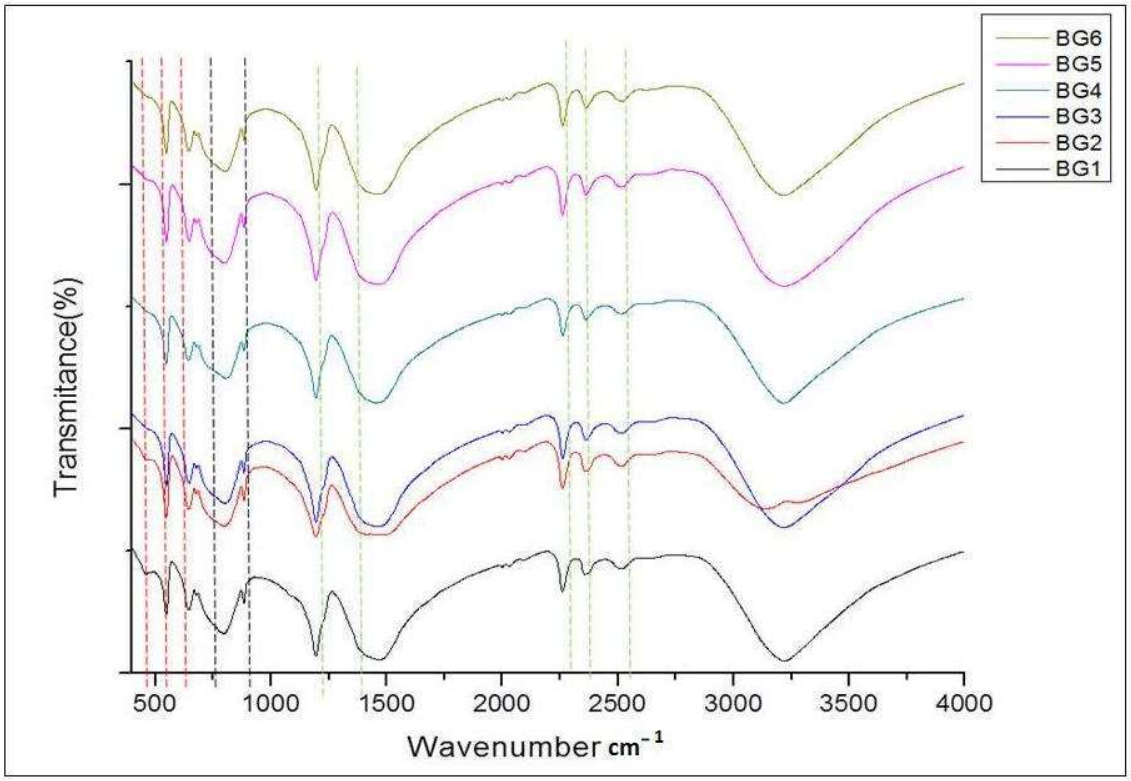


Figure 5.21: FTIR spectra of different glass sealant with different SiO_2/B_2O_3 ratio

At infrared spectra region between (700-810 cm^{-1}) antisymmetric stretching of Si-O-Si in (SiO4) tetrahedral unit was observed. The B-O band stretching was observed in the tetrahedral group of (BO_4) corresponding to (900-1200 cm^{-1}) infrared spectra region. An asymmetric stretching relaxation of B-O bond in the trigonal units in the infrared spectra region of (1200-1400 cm^{-1}) was observed. The intensity of bond at 1400cm^{-1} decreased from (BO_4 to BO_3) due to increasing of SiO_2/B_2O_3 Ratio of glass sealant. Whereas, the increase in the ratio of SiO_2/B_2O_3 (SiO_2 to SiO_4) tetrahedral unit was enhanced. The presence of SiO_4 and BO_4 increasing the continuity of glass network. [Yingling.et.al 2015] studied the borosilicate glass and found similar SiO_4 tetrahedral unit, BO_4 tetrahedral unit and BO_3 trigonal unit in borosilicate glass system. The assignment of different transmittance bond observed in the spectra of different glass system reported by the researcher [Rada et.al ,2006] is shown in Table 5.2.

[Elegilli.K,2003] has studied that the amount of SiO_2 replaced by B_2O_3 when the content of Na_2O and Al_2O_3 were constant which results in the increase in the [BO_4] tetrahedral unit content and reduction in [BO_3] as a result of which network structure becomes dense which decreases the coefficient of thermal expansion of glass.

5.3.5 Effect of SiO_2 / B_2O_3 Ratio on Thermal Properties of Glass Sealant

The presence of [BO_4] in glass sealant system by increasing the SiO_2/B_2O_3 Ratio increases it transition temperature Tg and crystallization temperature Tc. The glass transition temperature and crystallization curve of different glass sealant is as shown in Figure 5.22. The borosilicate family glass contains SiO_2, B_2O_3, Na_2O, and Al_2O_3. The SiO_2 has higher melting temperature as compared to B_2O_3 having of low thermal expansion. B_2O_3 in glass system act as the useful modifier which can decrease the melting temperature of glass sealant. The addition of B_2O_3 in borosilicate glass sealant by decreasing the SiO_2 while keeping the percentage of Al_2O_3 and Na_2O constant decreases the melting temperature of glass sealant as shown in Figure 5.26. The DTA peaks below 200 °C two peaks were obtained which is because of the evaporation of moisture from the glass sealant specimen shown in Figure 5.22. The calculation of glass transition temperature was carried, on the basis of glass sealant powder heat capacity (the amount of heat it takes to raise the temperature of sealant by one degree. The glass transition temperature was calculated where endothermic peak (glass sealant absorbed heat from the

surrounding) was observed. The smaller peak corresponding between 500 °C to 600 °C shows the glass transition temperatures Tg whereas smaller peak between 700 °C to 830 °C shown the crystallization temperature Tc shown in Figure 5.22. The glass transition Tg and crystallization temperature Tc of glass sealant decreased as SiO_2/B_2O_3 Ratio decreased. The decrease in the SiO_2/B_2O_3 Ratio of glass sealant confirmed that replacing the SiO_2 content with B_2O_3 decreases the glass transition temperature and crystallization temperature.

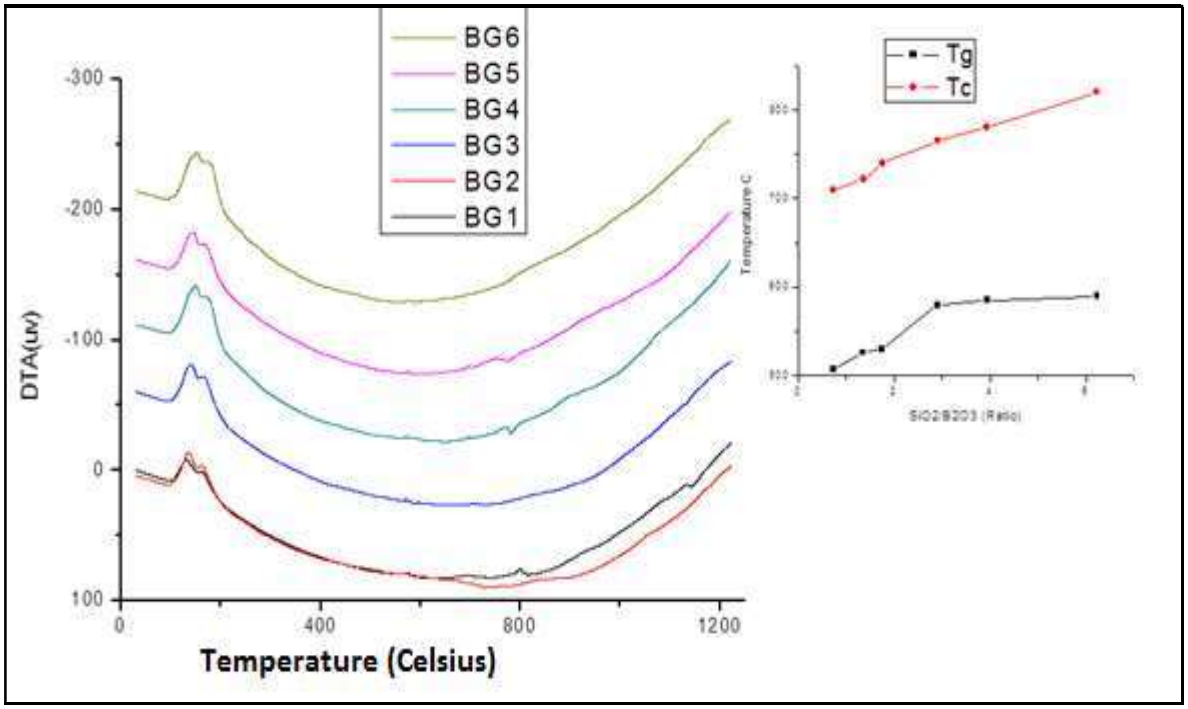


Figure 5.22: DTA curve of different glass sealant with respect to temperature and Tg, Tc variation with different SiO_2/B_2O_3 ratio

The percentage weight loss of different glass sealant with different SiO_2/B_2O_3 Ratio is shown in Figure 5.23. The weight loss of glass sealant decreased as SiO_2/B_2O_3 Ratio decreased. The maximum weight loss was observed in glass sealant corresponding to maximum SiO_2/B_2O_3 Ratio 6.8. The maximum weight loss was observed because of the presence of high weight percentage of B_2O_3 as compared to SiO_2.The maximum weight loss for all glass sealant specimens was obtained below 200 °C, which was occur because of the evaporation of moisture from the glass sealant specimen. The weight loss remains straight till 500 °C and then weight loss starts decreasing because of the glass transition temperature. As temperature increased further above 700 °C slight changes in weight was obtained which occur due to the crystallization of the glass sealant as shown in Figure 5.23. The percentage weight loss of glass sealant decreased as SiO_2/B_2O_3 Ratio decreased which was occur due of the increase in density of glass sealant as SiO_2/B_2O_3 Ratio decreased.

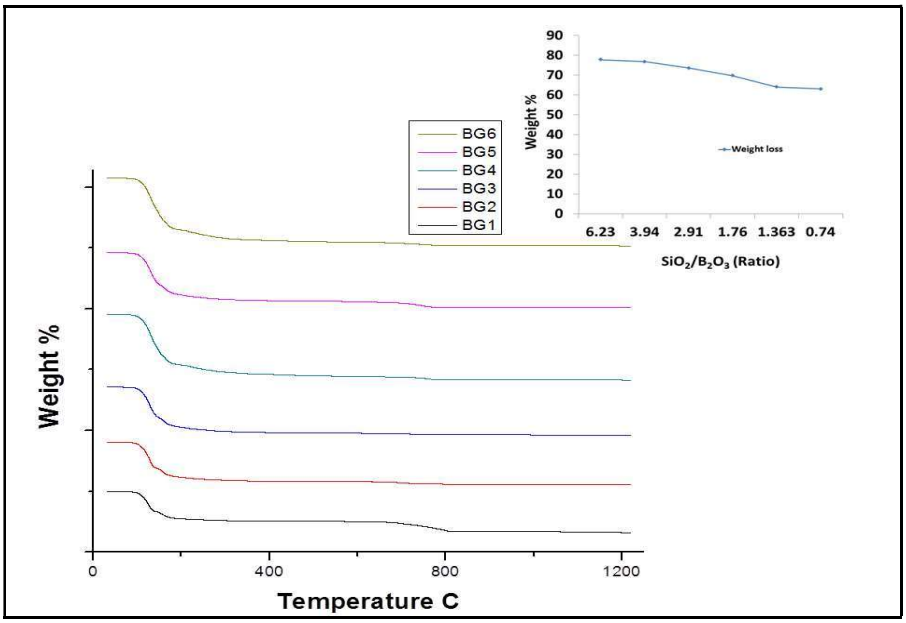


Figure 5.23: Percentage weight loss curve for different specimen and weight loss with different SiO_2/B_2O_3 ratio

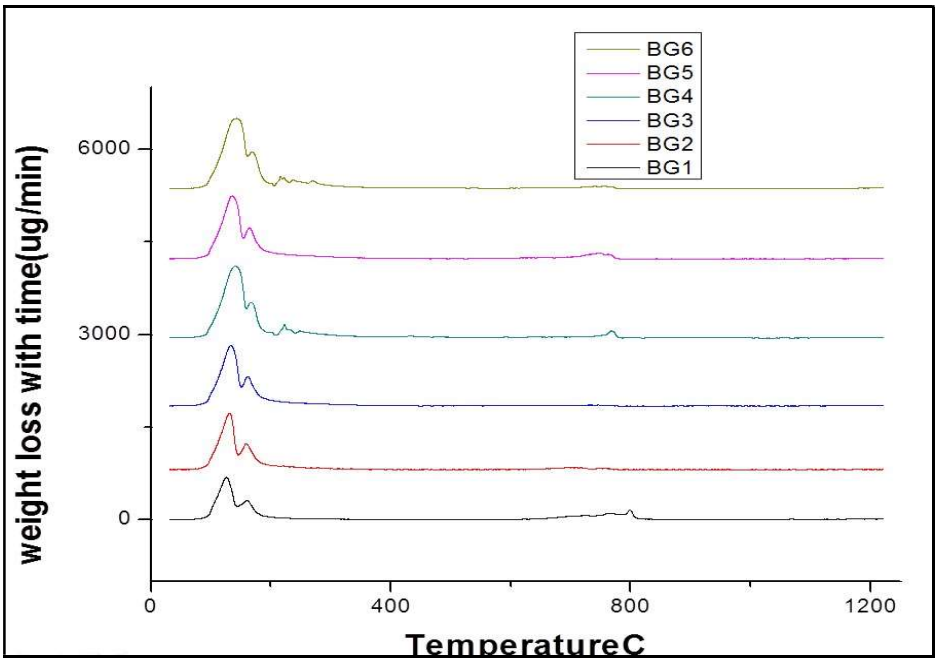


Figure 5.24: Weight loss per minutes with respect to temperature

The weight loss per unit time below 200 °C was observed because of the evaporation of moisture from the glass sealant specimen. The lower weight loss change with respect to time was observed between 700 °C to 800 °C shown in Figure 5.24 which show the confirming the start of crystallization of glass sealant.

5.3.6 Effect of SiO_2 / B_2O_3 Ratio on Thermal Conductivity of Glass Sealant

The thermal conductivity of glass sealant increased with the decrease in SiO_2/B_2O_3 Ratio decreases. The variation of thermal conductivity of glass sealant with different SiO_2/B_2O_3 Ratio is shown in Figure 5.25.

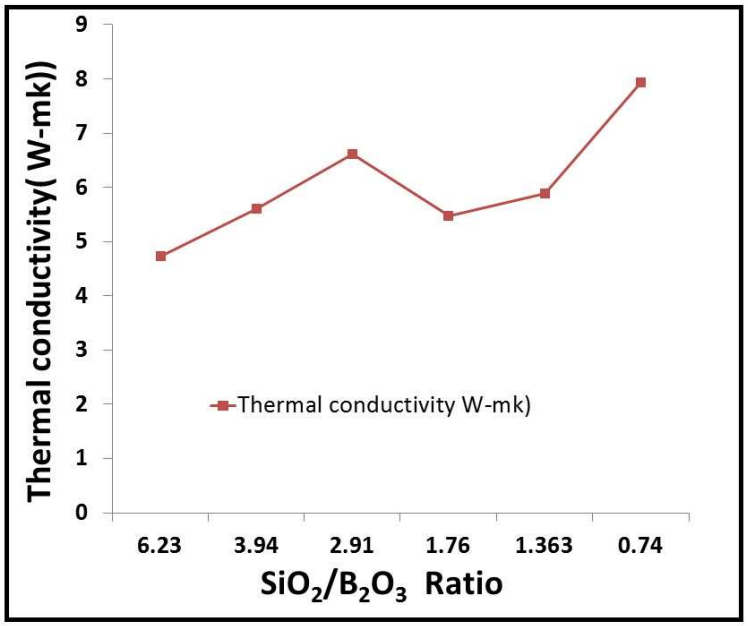


Figure 5.25: Thermal conductivity of glass sealant with different SiO_2/B_2O_3 ratio

5.3.7 Effect of SiO_2 / B_2O_3 Ratio on SEM/EDAX Analysis of Glass Sealant

The micrographs of different glass sealants after melting are shown in Figure 5.26 (a-f).

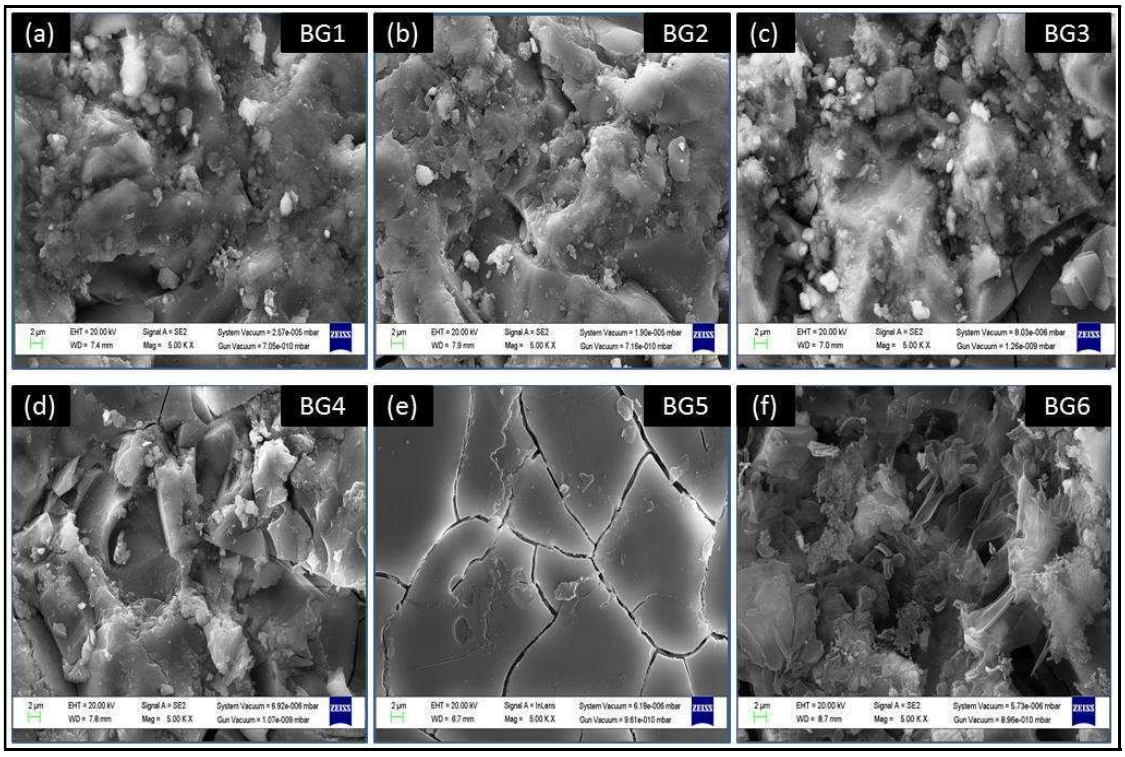


Figure 5.26: Scanning electron micrograph of glass sealants with respect to decreasing SiO_2/B_2O_3 ratio

The SEM images of glass sealants were taken at a magnification of 5000X on a scale of 2µm. The BG1 glass as shown in Figure 5.26 (a) shows the improper melting of glass sealant because of the higher percentage of SiO_2 content as compared to B_2O_3. The higher percentage of SiO_2 makes glass to melt at high temperature whereas B_2O_3 content in the SiO_2 makes glass to melt at a lower temperature.

The morphology of glass sealant with decreasing SiO_2/B_2O_3 is shown in Figure 5.26 (a-f). The percentage of an undissolved particle of the glass sealant start decreasing as SiO_2/B_2O_3

decreases. The uniform melting of glass sealant decreases its melting temperature and contact angle. As a result of this, wettability of glass sealant increases as shown in Figure 5.17 in BG6 specimen. The change in percentages composition of different elements obtained through EDAX analysis with respect to different SiO_2/B_2O_3 is shown in Figure 5.27 (a-f).

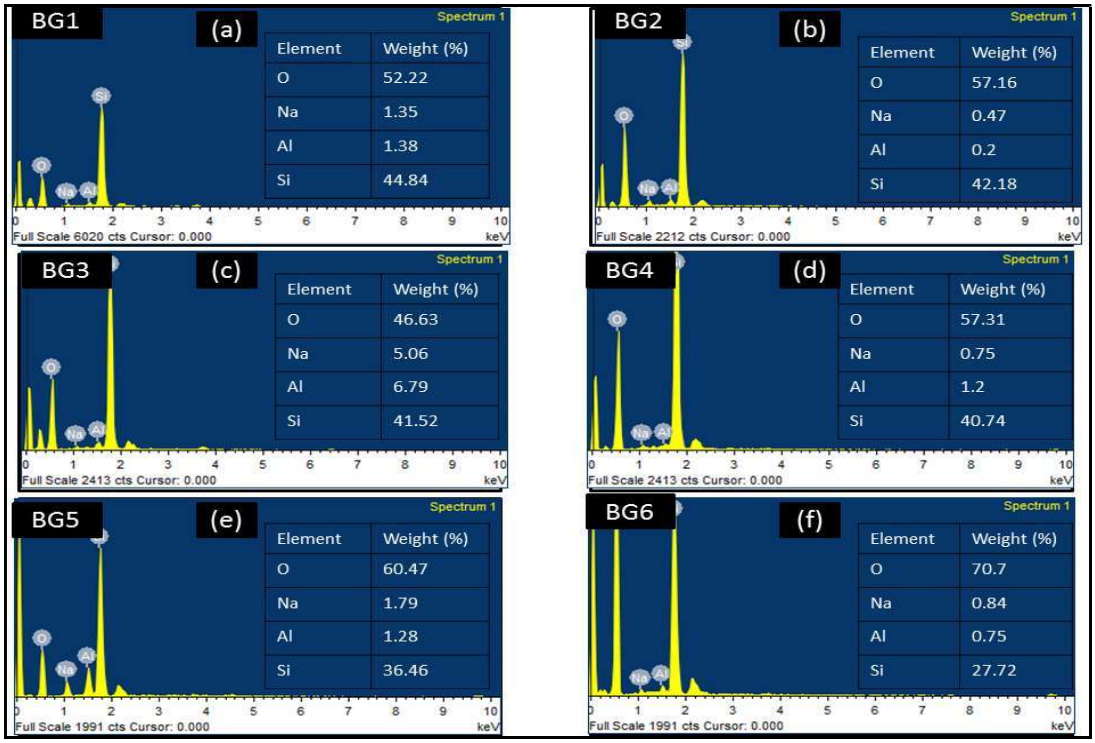


Figure 5.27: EDAX of glass sealants with respect to decreasing SiO_2/B_2O_3 ratio

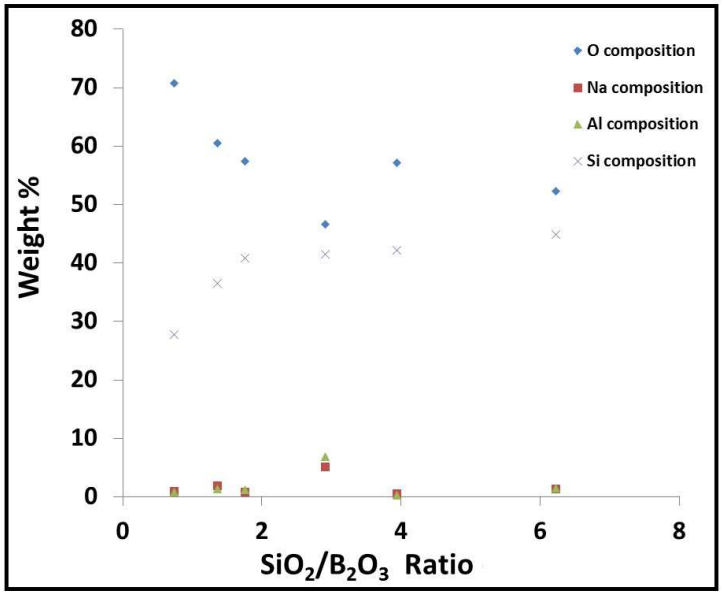


Figure 5.28: Elemental composition of different glass sealant with different SiO_2/B_2O_3 ratio

The elemental composition of O element increased with the decrease in SiO_2/B_2O_3 ratio, which occurred because of the addition of B_2O_3. The elemental composition of Al and Na were almost same corresponding to different SiO_2/B_2O_3 ratios shown in Figure 5.28 which is due to the addition of same weight percentages of Al_2O_3 and Na_2O during the formation of different glass sealant powder. The percentage of Si decreased with the decrease in SiO_2/B_2O_3 ratio as shown in Figure 5.28. The lower percentage of Si as SiO_2/B_2O_3 decreased was obtained because of the lower weight percentage of SiO_2 as compared to B_2O_3 weight percentage during the formation of different glass sealant.

5.4 GLASS SEALANT RESULTS OBTAINED THROUGH DESIGN OF EXPERIMENT METHODOLOGY

The composition was further tailored by using mixture design methodology and taking BG6 specimen glass sealant composition which was obtained through SiO_2/B_2O_3 ratio. The wettability, adhesion strength, glass transition temperature, crystallization temperature, density and thermal conductivity were examined according to design matrix as shown in (Table 4.4.)

5.4.1 Result and Regression Models

The X-ray diffraction pattern of different glass sealant is shown in Figure 5.29. In XRD pattern of glass sealant specimen, no peak was observed which confirmed the amorphous nature of the glass sealant specimen.

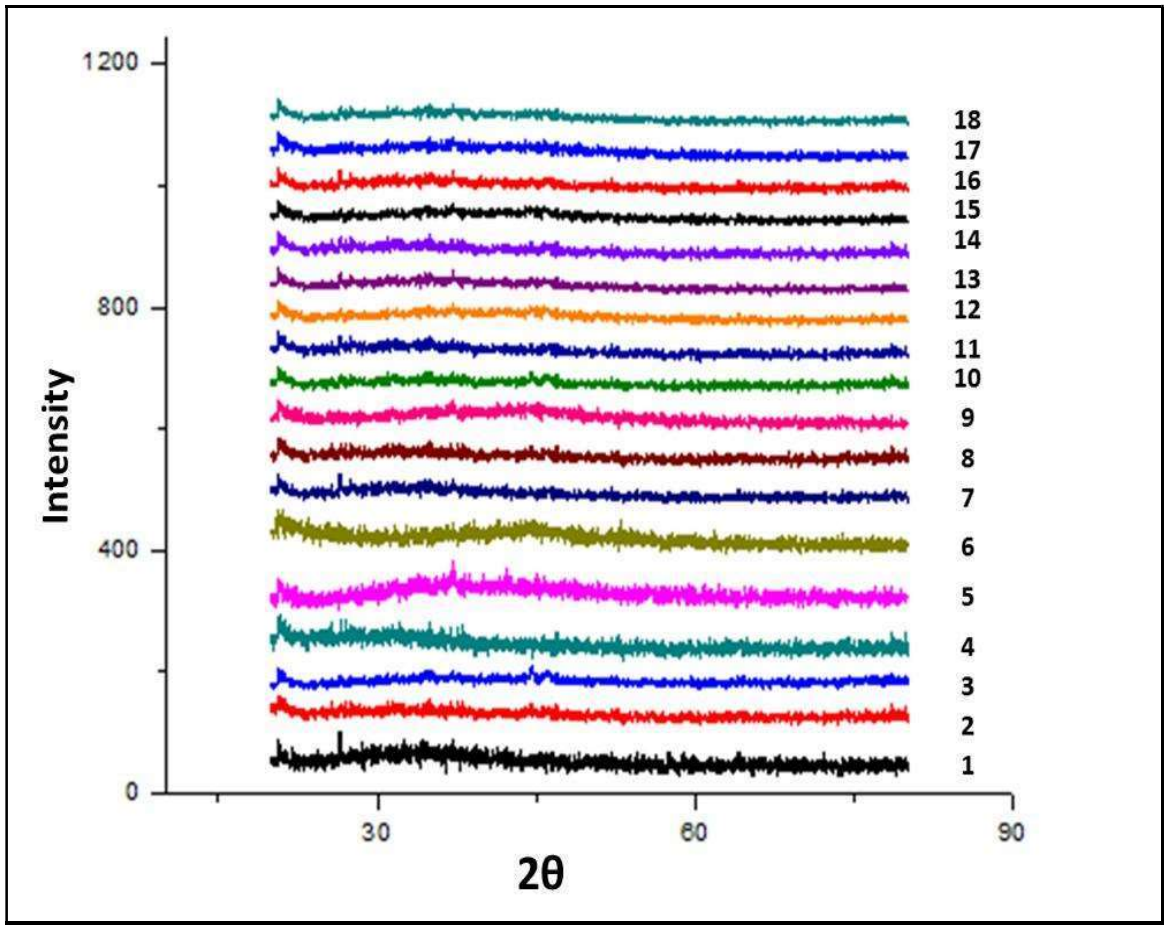


Figure 5.29: X-Ray Diffraction pattern of glass sealant specimen

The output response of glass sealant obtained through thermal studies, i.e. thermal conductivity, glass transition temperature, weight loss and crystallization temperature are shown in Table 5.3. The output response of glass sealants such as contact angle, spreading area, and density given in Table 5.4.

Table 5.3: Output response of glass sealant obtained though thermal studies

Experiment Number	Tg °C	Tc °C	Thermal conductivity (W-mk)	Percentage weight loss
1	650	752	6.6	75.54
2	580	695	3.8	74.46
3	690	793	7.0	70.29
4	657	787	4.9	78.47
5	600	691	6.1	72.78
6	663	781	6.2	72.1
7	602	705	3.2	71.4
8	662	785	6.4	73.1
9	665	775	5.8	70.8
10	707	810	6.9	62.7
11	646	740	8.6	73.5
12	740	850	6.7	78.7
13	720	830	7.6	68.5
14	601	760	5.6	77.9
15	590	740	6.2	77.5
16	703	815	5.00	69.6
17	691	800	6.2	71.9
18	660	780	4.7	76.4

Table 5.4: Wetting, spreading and density response of glass sealant

Experiment Number	Contact angle (θ)	Spreading Area(mm^2)	Density (g/cm^3)
1	20.2	397.4	1.9
2	18.9	452.2	1.6
3	34.2	298.5	2.2
4	42.5	254.3	1.9
5	12.5	593.7	1.7
6	41.9	262.9	1.8
7	29.0	593.7	1.6
8	44.6	262.9	1.3
9	28.2	251.5	2.1
10	59.1	176.6	1.7
11	18.9	346.2	1.0
12	70.6	113.0	1.5
13	68.2	132.7	1.0
14	16.7	551.3	1.1
15	9.7	683.1	1.9
16	21.1	201.0	1.4
17	38.9	226.9	2.0
18	36.9	254.3	1.3

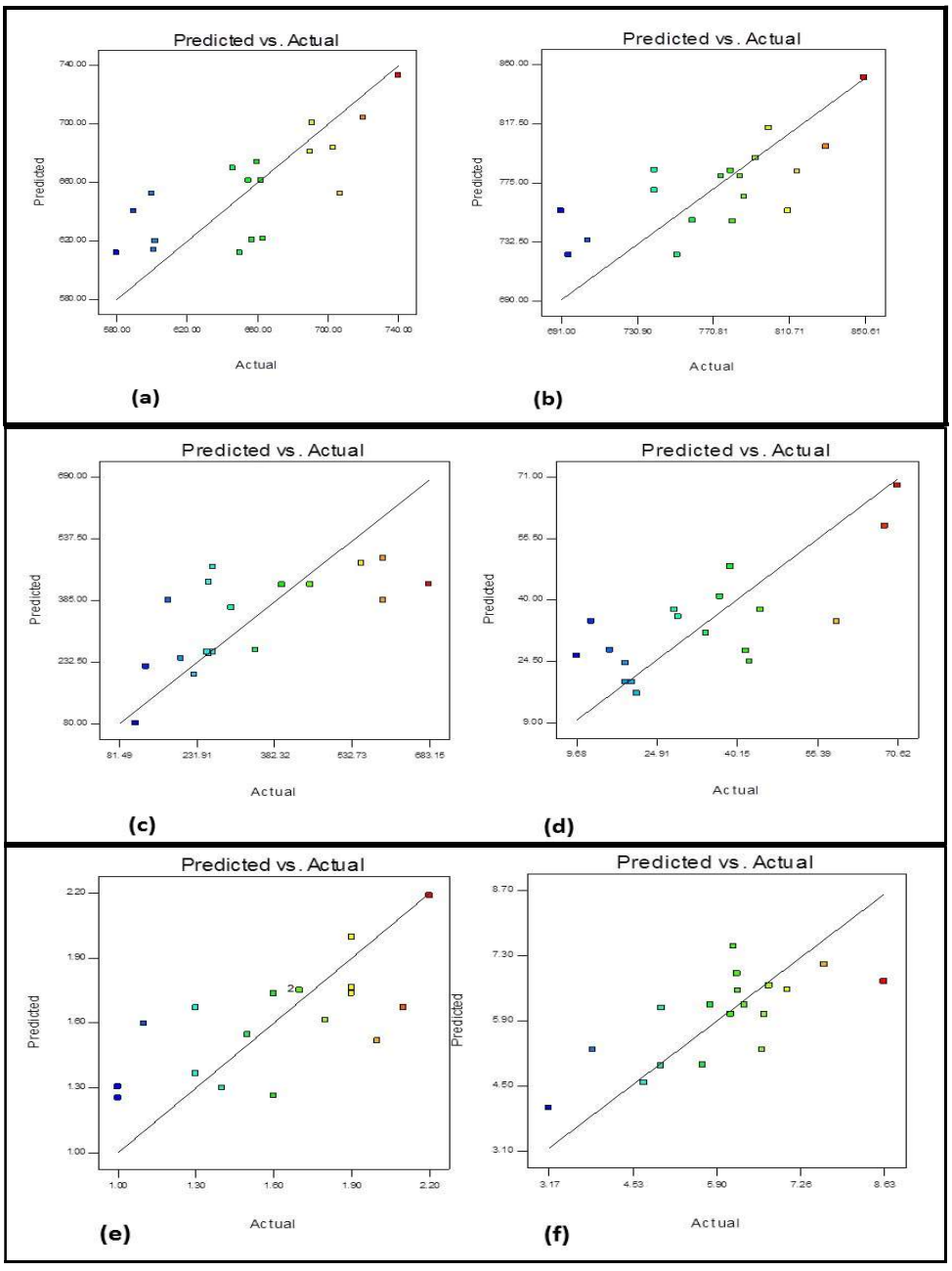
With the help of observed output response in term of contact angle, spreading area, thermal conductivity, glass transition temperature Tg, crystallization temperature Tc and percentage weight loss, the regression equation developed in term of percentage composition of glass

sealant component (SiO_2, Al_2O_3 , Na_2O and B_2O_3) and their combined binary mixture are shown in Appendix A1(Table A1).

The regression equations developed in Appendix 1 (A1-A7) was analyzed using analysis of variance (ANOVA) as shown in Appendix 1 (Table A1) shows the analysis of regression equation of glass sealant response. The R square value shown in the table for the developed regression model obtained nearly equal or greater than 84 % which indicate the predicted value was close agreement with the actual value of various output response of glass sealant shown in Figure 5.30(a-g).

5.4.2 Effect of Glass Constituent on the Properties of Glass Sealant

The result obtained through output response shows that the glass transition temperature Tg and crystallization temperature Tc of glass sealant increase as the SiO_2 content increases. The increase in Tg and Tc of glass sealant reduces the wettability of glass sealant over the metal specimen as a result of these contact angle of glass sealant increases. The spreading area of glass sealant was also decreased as SiO_2 content increased. The actual and predicted value plot of Tg, Tc, spreading area, contact angle, density, thermal conductivity and percentage weight loss are shown in Figure 5.30 (a-g).



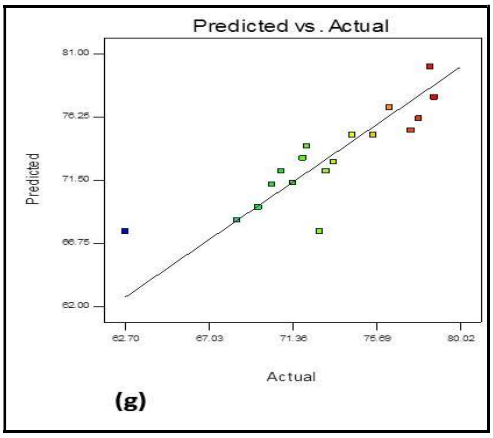


Figure 5.30: Predicted versus actual values of various glass sealant response (a)Tg ,(b) Tc,(c) Spreading area,(d) Contact angle, (e) Density , (f) Thermal Conductivity, (g) Percentage weight loss

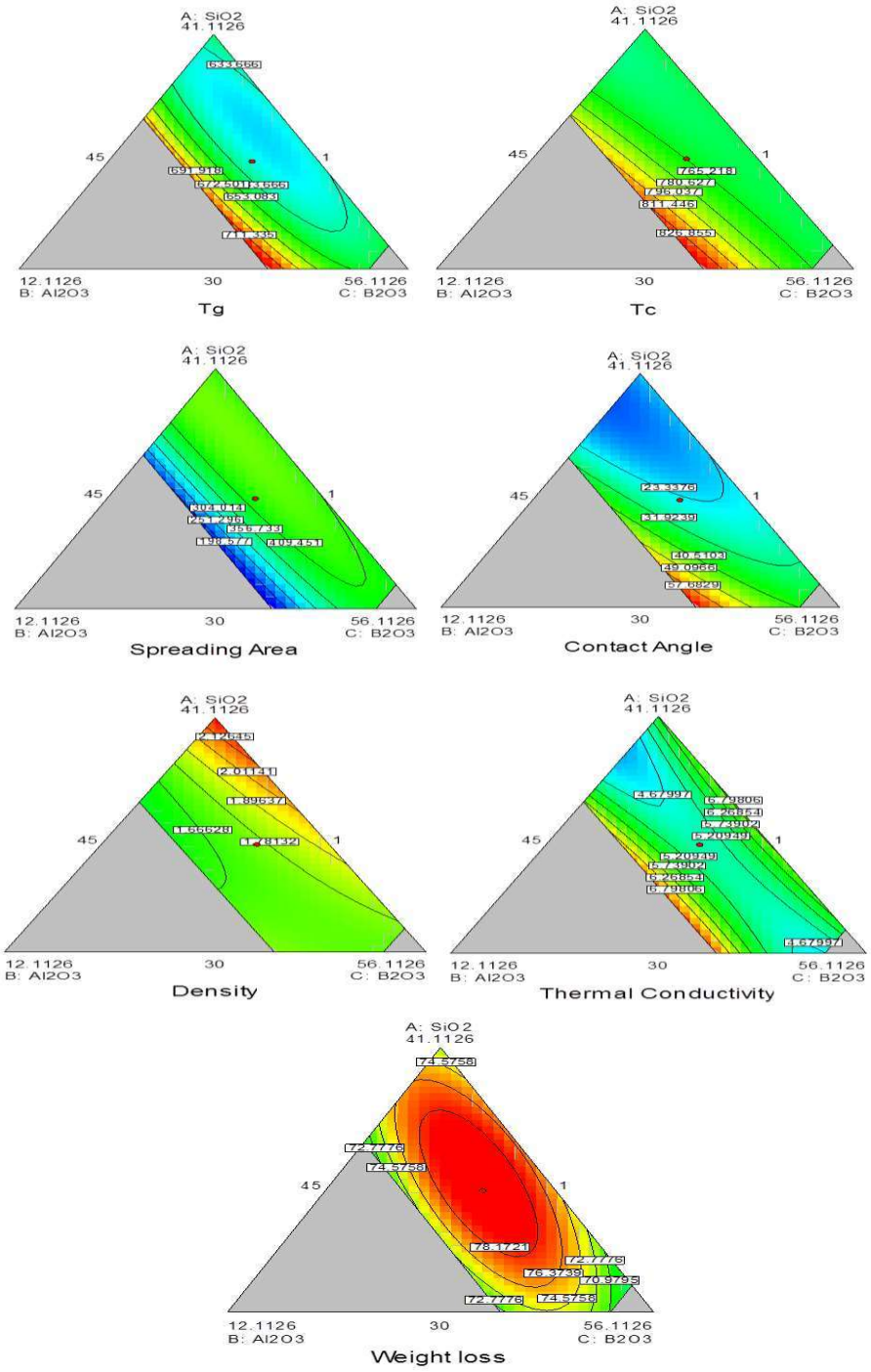
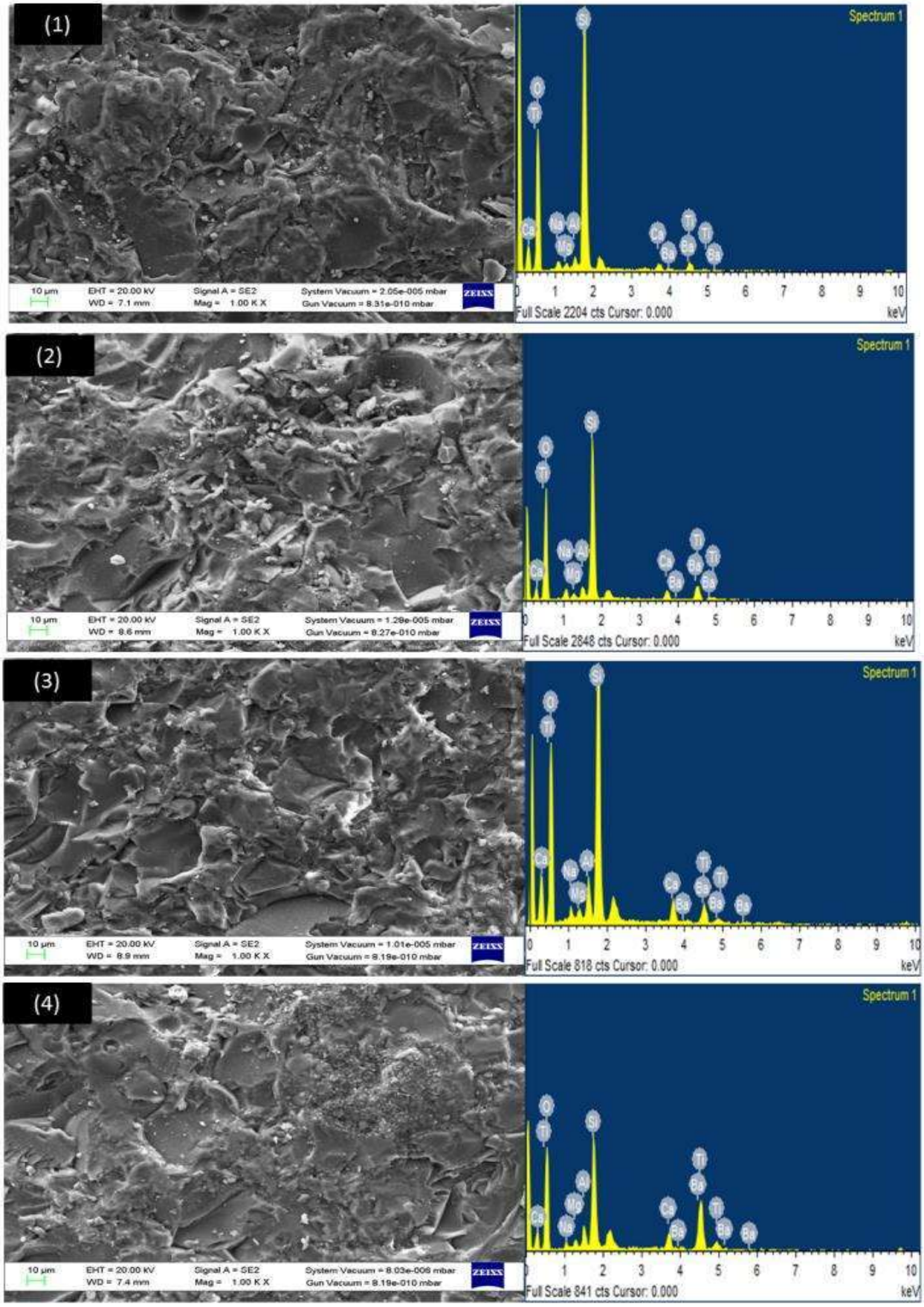
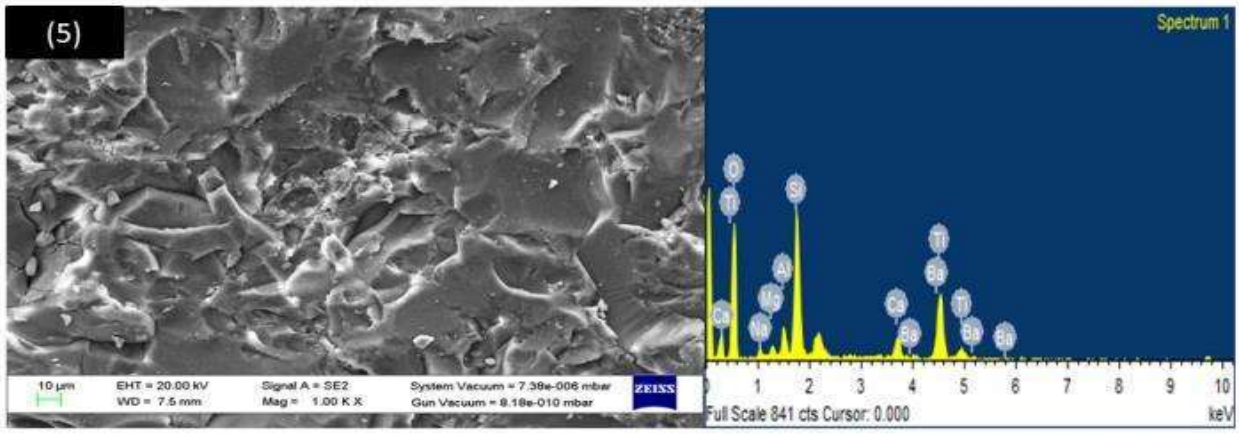
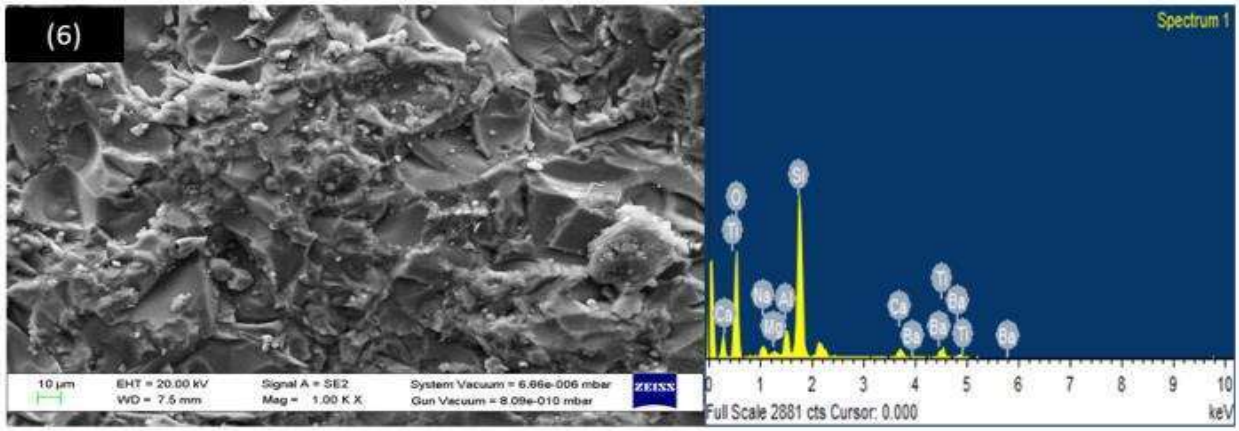


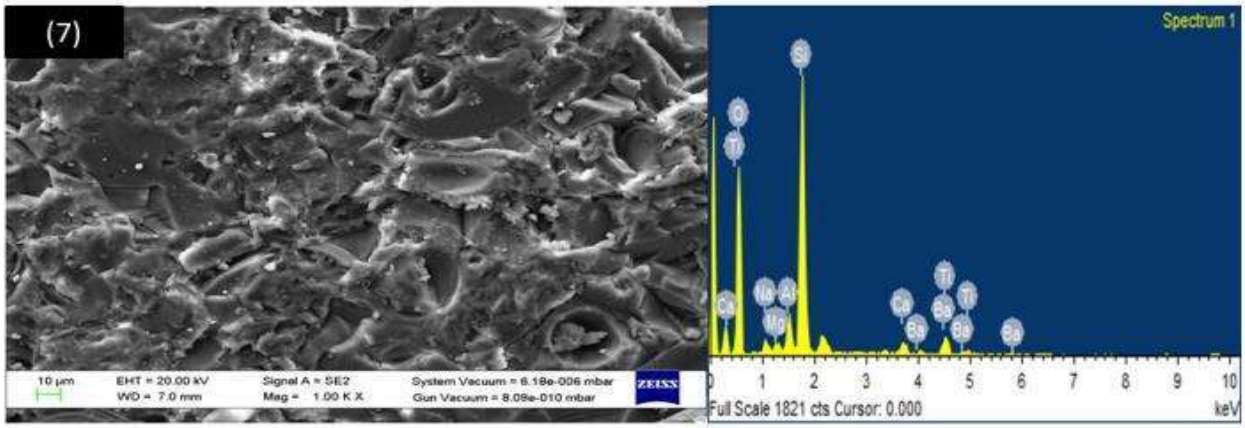
Figure 5.31: Contour surface plots for various glass sealant response (a)Tg ,(b) Tc,(c) Spreading area,(d) Contact angle, (e) Density , (f) Thermal Conductivity, (g) Percentage weight loss

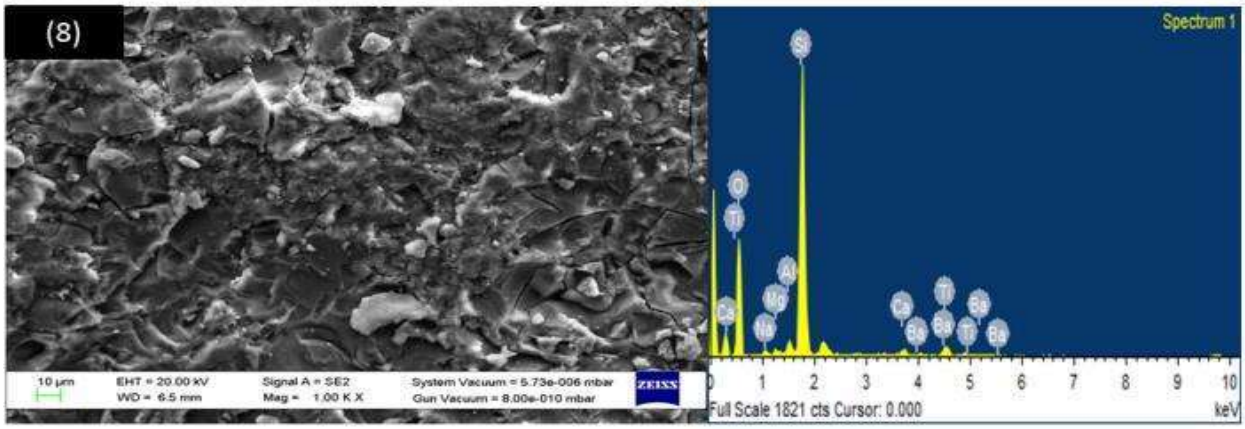
The contour surface plot of glass sealant response is shown in Figure 5.31 (a-h). The maximum limit of SiO_2, Al_2O_3, and B_2O_3 were taken as 41.1126, 12.1126 and 56.1126 respectively.

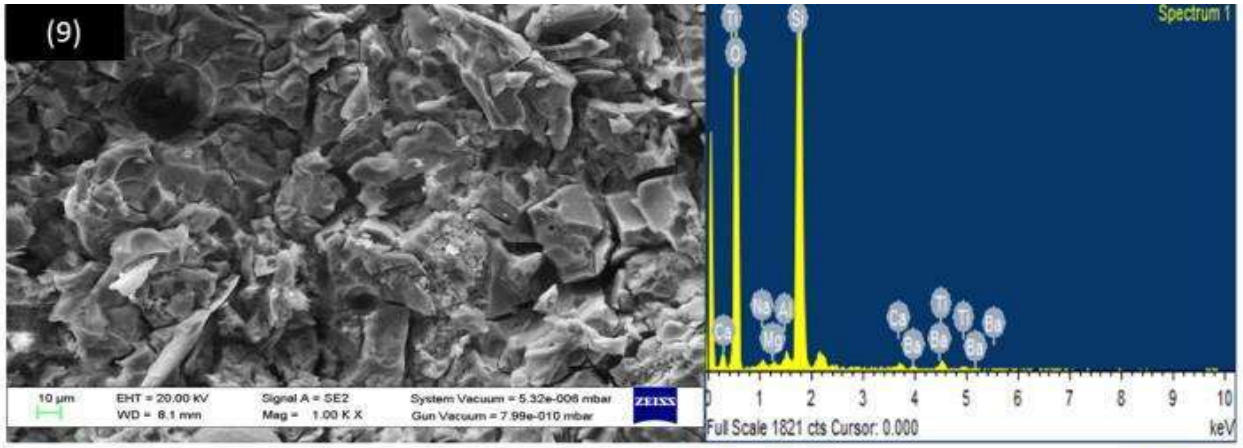


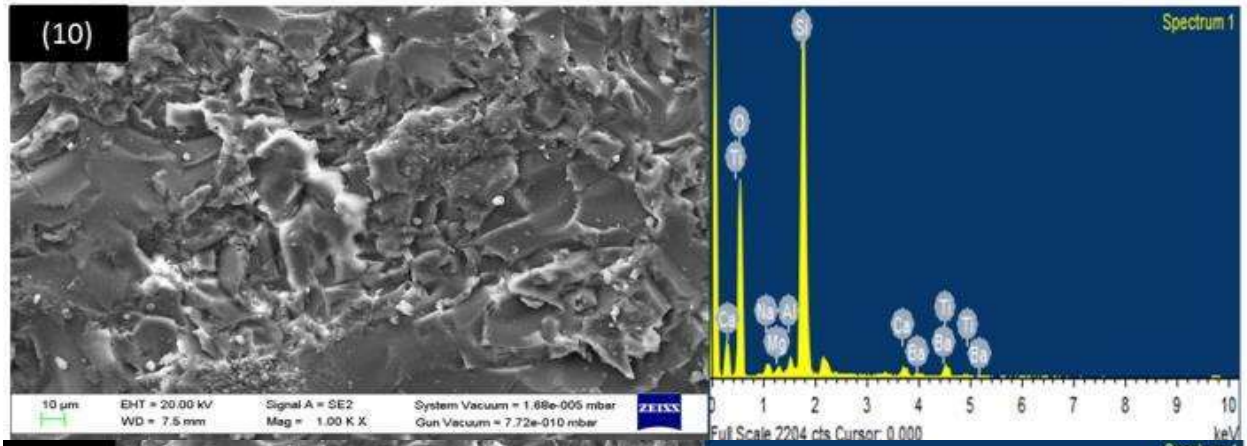

(5)
Spectrum 1
10 µm
EHT = 20.00 kV
WD = 7.5 mm
Signal A = SE2
Mag = 1.00 K X
System Vacuum = 7.38e-006 mbar
Gun Vacuum = 9.18e-010 mbar
ZEISS
Full Scale 841 cts Cursor: 0.000
keV

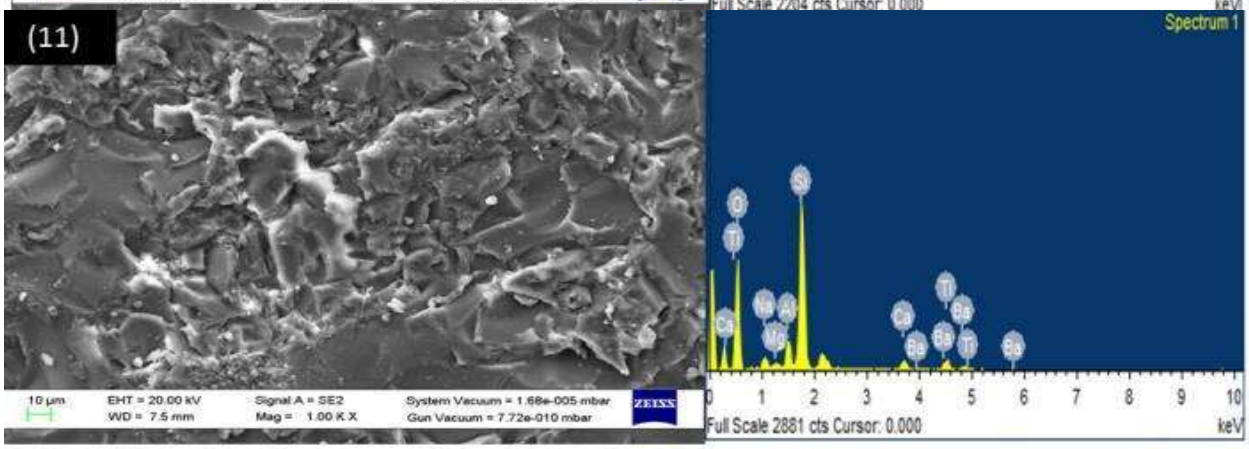

(6)
Spectrum 1
10 µm
EHT = 20.00 kV
WD = 7.5 mm
Signal A = SE2
Mag = 1.00 K X
System Vacuum = 6.66e-006 mbar
Gun Vacuum = 8.09e-010 mbar
ZEISS
Full Scale 2881 cts Cursor: 0.000
keV

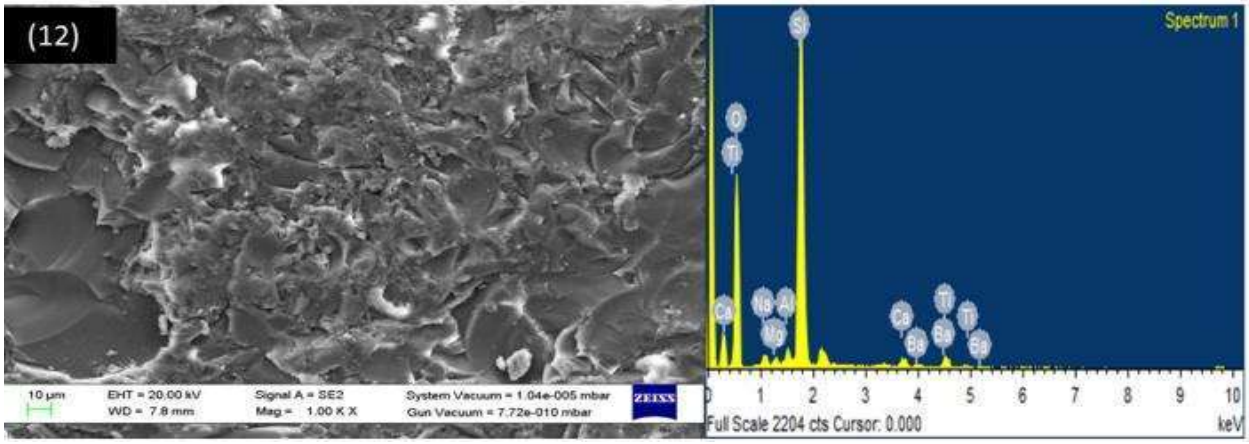

(7)
Spectrum 1
10 µm
EHT = 20.00 kV
WD = 7.0 mm
Signal A = SE2
Mag = 1.00 K X
System Vacuum = 6.18e-006 mbar
Gun Vacuum = 8.09e-010 mbar
ZEISS
Full Scale 1821 cts Cursor: 0.000
keV

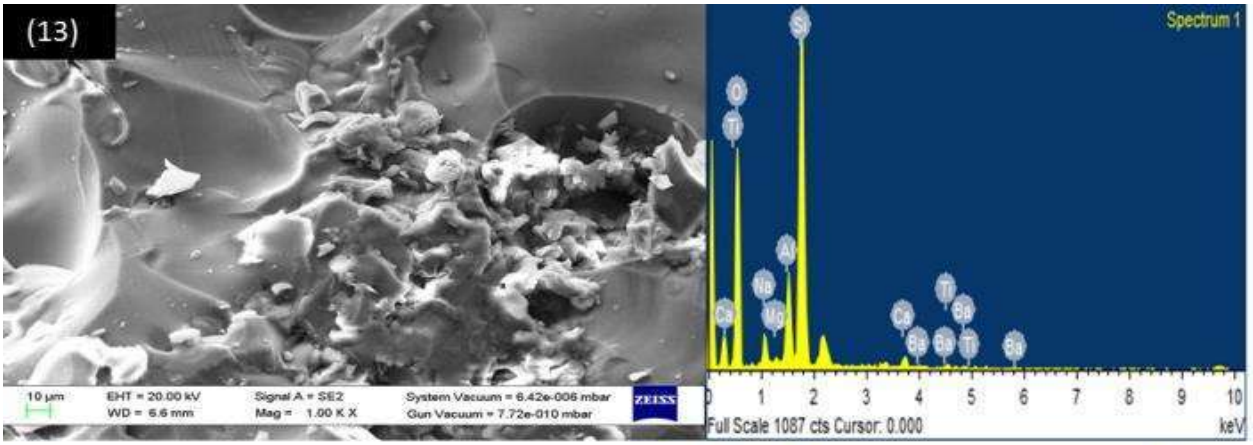

(8)
Spectrum 1
10 µm
EHT = 20.00 kV
WD = 6.5 mm
Signal A = SE2
Mag = 1.00 K X
System Vacuum = 5.73e-006 mbar
Gun Vacuum = 8.00e-010 mbar
ZEISS
Full Scale 1821 cts Cursor: 0.000
keV

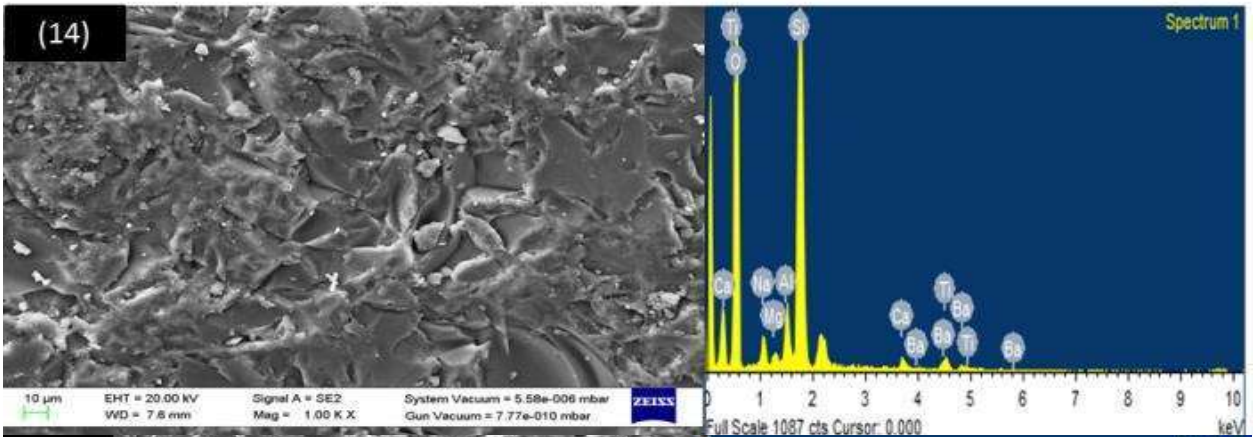

(9)
Spectrum 1
10 µm
EHT = 20.00 kV
WD = 8.1 mm
Signal A = SE2
Mag = 1.00 K X
System Vacuum = 5.32e-006 mbar
Gun Vacuum = 7.99e-010 mbar
ZEISS
Full Scale 1821 cts Cursor: 0.000
keV

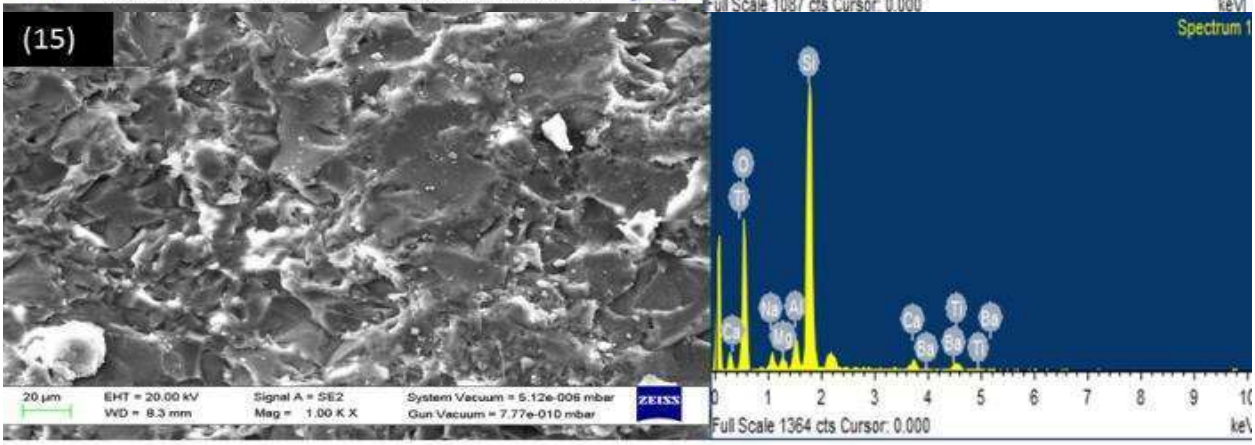

(10)
Spectrum 1
10 µm
EHT = 20.00 kV
WD = 7.5 mm
Signal A = SE2
Mag = 1.00 K X
System Vacuum = 1.68e-005 mbar
Gun Vacuum = 7.72e-010 mbar
ZEISS
Full Scale 2204 cts Cursor: 0.000
keV

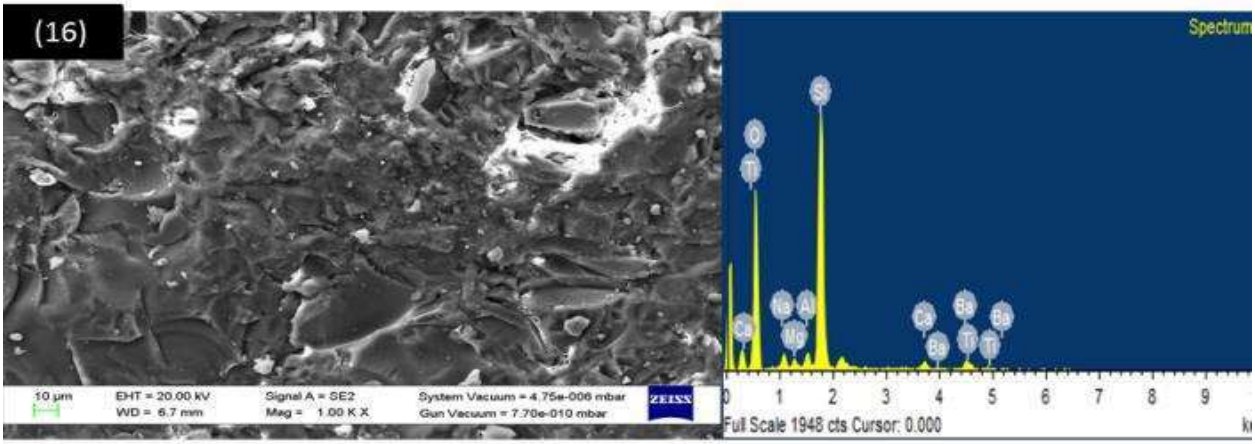

(11)
Spectrum 1
10 µm
EHT = 20.00 kV
WD = 7.5 mm
Signal A = SE2
Mag = 1.00 K X
System Vacuum = 1.68e-005 mbar
Gun Vacuum = 7.72e-010 mbar
ZEISS
Full Scale 2881 cts Cursor: 0.000
keV


(12)
Spectrum 1
10 µm
EHT = 20.00 kV
WD = 7.8 mm
Signal A = SE2
Mag = 1.00 K X
System Vacuum = 1.04e-005 mbar
Gun Vacuum = 7.72e-010 mbar
ZEISS
Full Scale 2204 cts Cursor: 0.000
keV


(13)
Spectrum 1
10 µm
EHT = 20.00 kV
WD = 6.6 mm
Signal A = SE2
Mag = 1.00 K X
System Vacuum = 6.42e-006 mbar
Gun Vacuum = 7.72e-010 mbar
ZEISS
Full Scale 1087 cts Cursor: 0.000
keV


(14)
Spectrum 1
10 µm
EHT = 20.00 kV
WD = 7.6 mm
Signal A = SE2
Mag = 1.00 K X
System Vacuum = 5.58e-006 mbar
Gun Vacuum = 7.77e-010 mbar
ZEISS
Full Scale 1087 cts Cursor: 0.000
keV


(15)
Spectrum 1
20 µm
EHT = 20.00 kV
WD = 8.3 mm
Signal A = SE2
Mag = 1.00 K X
System Vacuum = 5.12e-006 mbar
Gun Vacuum = 7.77e-010 mbar
ZEISS
Full Scale 1364 cts Cursor: 0.000
keV


(16)
Spectrum
10 µm
EHT = 20.00 kV
WD = 6.7 mm
Signal A = SE2
Mag = 1.00 K X
System Vacuum = 4.75e-006 mbar
Gun Vacuum = 7.70e-010 mbar
ZEISS
Full Scale 1948 cts Cursor: 0.000

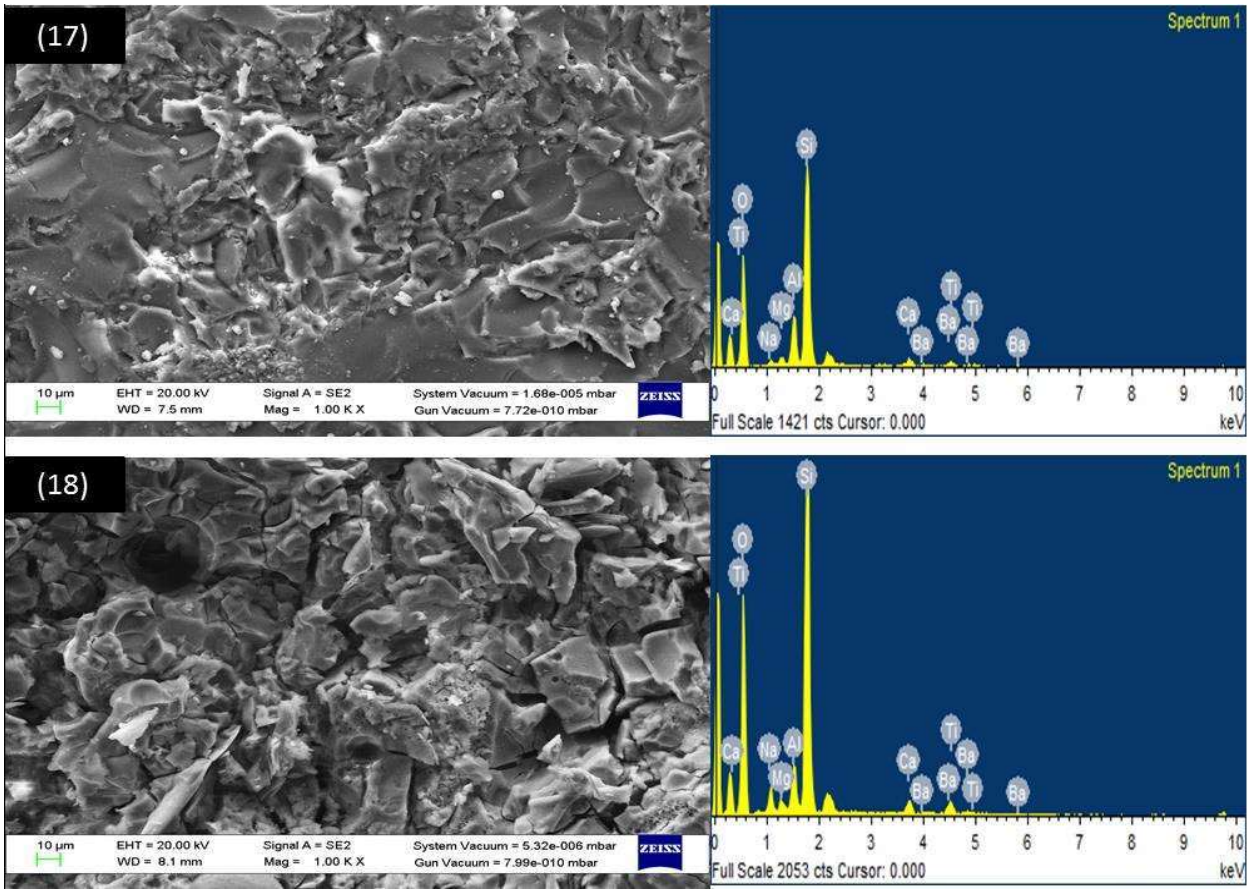


Figure 5.32 (1-18): Scanning electron micrograph and Energy dispersive X-rays Image of glass sealant specimens

The addition of Al_2O_3 in glass sealant increased, the glass transition temperature Tg and crystallization temperature Tc of glass sealant which increases the contact angle formed by glass sealant over the metal specimen and reduces the spreading behavior of glass sealant

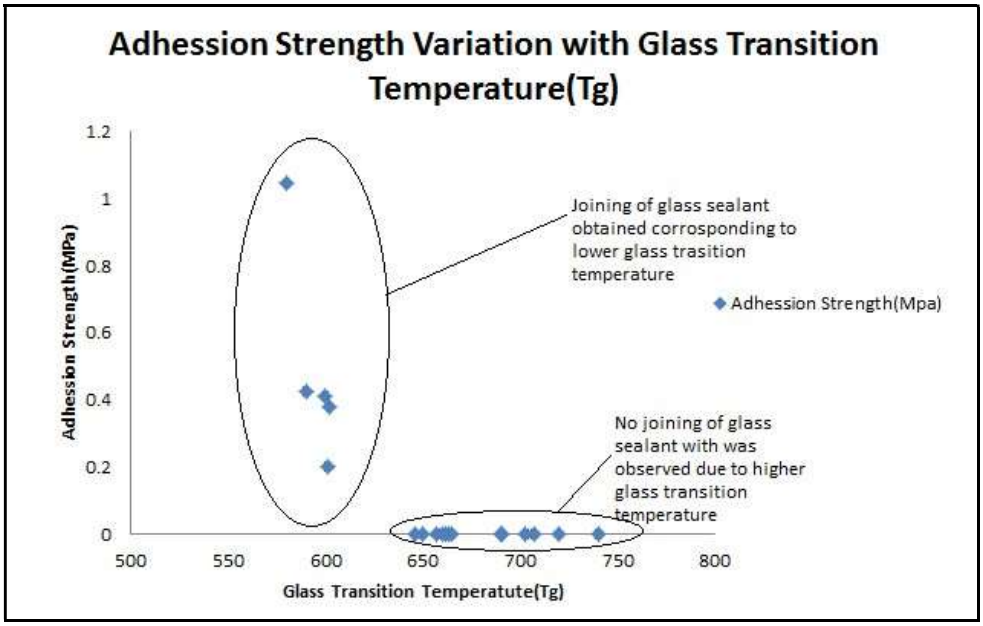


Figure 5.33: Adhesion strength variation with glass transition temperature (Tg)

.Whereas the addition of B_2O_3 in glass sealant system decreased the glass transition temperature Tg and Tc. The B_2O_3 in glass sealant system act as a network modifier having lower melting point causes the improvement in glass sealant wetting properties over the metal specimen. The

presence of Na_2O in a glass sealant system acts as a flux which helps in lowering the melting temperature of SiO_2.

The addition of Na_2O in glass sealant decreased the glass transition temperature Tg and crystallization temperature of glass sealant Tc. The decrease in Tg and Tc of glass sealant reduces the value of contact angle and increases the spreading area and adhesion of glass with metal. The additions of Al_2O_3 in glass sealant system increased the thermal conductivity of glass sealant whereas addition of SiO_2 reduced the thermal conductivity of glass sealant. The morphology of glass sealants region at higher magnification 1000 X on the scale of 10 µm where the EDAX analysis was carried out is shown in Figure 5.32 (1-18).

The density of glass sealant also increased as SiO_2 and Al_2O_3 content in glass sealants were increased. On the other hand, the addition of B_2O_3 and Na_2O reduced the density of glass sealant. The increase in the density of glass sealant also reduced the percentage weight loss of glass sealant with the addition of SiO_2 and Al_2O_3 .Hence, the thermal stability of glass sealant was improved in terms of weight loss. The addition of B_2O_3 increased the percentage weight loss of glass sealant which caused the reduction of thermal stability of glass sealants. The results of glass sealant chemical compositions obtained after melting using EDAX analysis are shown in Table 5.5. The adhesion strength was observed maximum corresponding to lower glass transition temperature (Tg) where higher wettability was obtained. The joining of glass sealant specimen corresponding to higher glass transition temperature did not happen because of the lower wettability. The higher glass transition temperature of glass sealant makes the glass-metal joining difficult because glass tube melts before the melting of glass sealant, as a result no joint is possible. The condition of glass-metal joint because of higher glass transition temperature of glass sealant is shown in Figure 4.8. The adhesion strength variation with glass transition temperature is shown in Figure 5.33.

Table 5.5: Chemical composition of glass sealant pallet obtained after melting

Experiment Number	% Composition of glass sealant							
	O	Na	Mg	Al	Si	Ca	Ti	Ba
1	58.9	2.25	0.63	0.89	32.24	1.91	0.86	2.32
2	58.3	3.14	0.81	3.33	25.6	2.32	2.12	4.38
3	60.51	1.57	0.65	1.45	31.26	1.59	1.93	1.04
4	57.41	1.86	0.9	3.81	25.44	3.24	2.56	4.78
5	61.98	1.06	1.12	2.82	14.23	3.16	13.9	1.73
6	57.64	2.92	0.85	4.11	26.38	2.04	2.41	3.65
7	55.32	1.8	0.89	4.22	30.43	2.54	1.97	2.83
8	43.38	1.02	0.14	1.46	48.44	1.38	2.27	1.91
9	61.09	0.77	3	2.72	16.95	4.15	3.53	7.79
10	57.53	1.93	1.42	3.78	25.82	2.44	2.36	4.72
11	56.206	1.832	1.041	2.645	30.35	2.447	2.339	3.14
12	55.91	1.3	0.53	1.32	35.68	1.37	2.12	1.77
13	58.01	6.34	0.48	9.01	23.1	1.04	0.41	1.61
14	63.77	2.53	0.66	3.04	26.13	0.86	0.93	2.08
15	56.15	2	0.53	2.13	35.88	1.02	1.41	0.88
16	62.23	2.01	0.84	1.05	29.28	1.36	1.12	2.11
17	47.21	0.44	0.88	3.7	43.06	2.9	0.77	1.04
18	54.86	2.32	1.27	4.44	27	2.66	2.02	5.43

5.4.3 Model Validation

The developed regression models were validated by conducting the experiment on three different randomly selected chemical compositions of glass sealant. The output response results of experimentation and with regression model are shown in Table 5.6. From the experimentation and regression equation, it was observed that the results obtained with experimentation nearly matched with the results obtained through regression model with an error of even less than 5% in most of the cases.

Table 5.6: Error % in glass sealant compositions

Response	Glass Sealant Compositions								
	Glass sealant Compositon 1			Glass sealant Compositon 2			Glass sealant Compositon 3		
	SiO_2 Al_2O_3 B_2O_3 Na_2O 39 1 45 5			SiO_2 Al_2O_3 B_2O_3 Na_2O 33.5 5 48.5 3			SiO_2 Al_2O_3 B_2O_3 Na_2O 30 1 54 5		
	Predicted Value	Actual Value	Error(%)	Predicted Value	Actual Value	Error(%)	Predicted Value	Actual Value	Error(%)
Tg (°C)	618.97	650	4.92	572.78	601	4..69	670.35	703	4.64
Tc (°C)	721.96	752	3.99	729.6	760	4	779.8	815	4.3
Spreading Area ($mm^{2)}$	373.58	397.40	5.99	518.8	551.26	5.88	188.07	200	5.96
Contact angle (θ)	18.94	20.16	6.0	15.75	16.74	5.91	19.83	21.10	6.01
Density (g/cm^3)	1.808	1.9	4.84	1.049	1.1	4.63	1.3295	1.4	5.03
Thermal Conductivity (W-mk)	6.355	6.64	4.49	5.3938	5.67	4.87	4.7485	5.00	5.03
Weight loss %	72.47	75.54	4.06	74.86	77.9	3.89	66.75	69.5	4.13

Error %=((Actual value-Predicted value)/Actual value) ×100

5.4.4 Optimization of Glass sealant Composition

The optimization of glass sealant composition as per the requirement of fabricating glass-metal joint is shown in Table 5.7

Table 5.7: The optimized composition of glass sealant based on required objective

Response	**SiO_2**	**Al_2O_3**	**B_2O_3**	**Na_2O**	**Value**	**Desiriblity**	**Objective**
Tg (°C)	31.41 32.45 32.67	2.5 2.0 2.1	55 50.50 50.1	1 5 5	610 629 627	0.85 0.74 0.74	Minimize
Tc (°C)	31.70 30.60 35.15	2.2 3.5 1.9	55 54.45 47.92	1 1.38 5	721 754 748	0.83 0.71 0.68	Minimize
Spreading Area ($mm^{2)}$	31.8 33 38.6	2.2 1 2.1	55 55 46	1 1 5	524 490.84 438.84	0.80 0.74 0.64	Maximize
Contact angle (θ)	31.94 37.43 35.83	2.05 2.1 1.94	55 45.43 47.226	1 5 5	30.45 22.83 19.66	0.77 0.67 0.66	Minimize
Density (g/cm^3)	34.37 35.51 36.88	1.87 1.94 1.94	51.724 47.597 47.228	2.0 3.9 3.9	1.70 1.82 1.83	0.67 0.65 0.65	Maximize
Thermal Conductivity (W-mk)	38.154 33.130 35.140	2.11 2.16 2.134	45 53 43	4.630 1.67 2.378	3.71 4.91 3.94	0.672 0.66 0.64	Minimize
Weight loss (%)	31.74 32.44 30.45	1.6 1 2.31	55 55 55	1.62 1.55 2.634	69.87 67.81 71.09	0.64 0.627 0.59	Minimize

Three optimized chemical composition of all the responses were taken in to the level of desirability. The optimized glass sealant chemical compositions based on the requirement of glass sealant, having lower value glass transition temperature Tg, crystallization temperature Tc, contact angle, thermal conductivity and %weight loss and having higher spreading area and density.

5.5 PRE-OXIDATION TEMPERATURE OF SS304 METAL SPECIMEN

The oxide layer mass gain of metal specimen measured at a different pre-oxidation time and the pre-oxidation temperature is shown in Figure 5.34. The oxide layer mass gain of SS304 metal specimen increased with increase in oxidation time (2, 3, 4, 5 minutes) at 700 °C. As pre-oxidation temperature increases above 700 °C the oxide layer mass gain increased. The optimum oxide layer thickness on metal specimen varies with the type of metal. The oxide layer mass gain for austenitic stainless steel substrate was observed to be in range of (2.09×10^{-4} g/cm^2 to 9.45×10^{-4}g/cm^2) at 700 °C pre-oxidation temperature and for pre-oxidation time intervals 2, 3, 4 and 5 minutes.

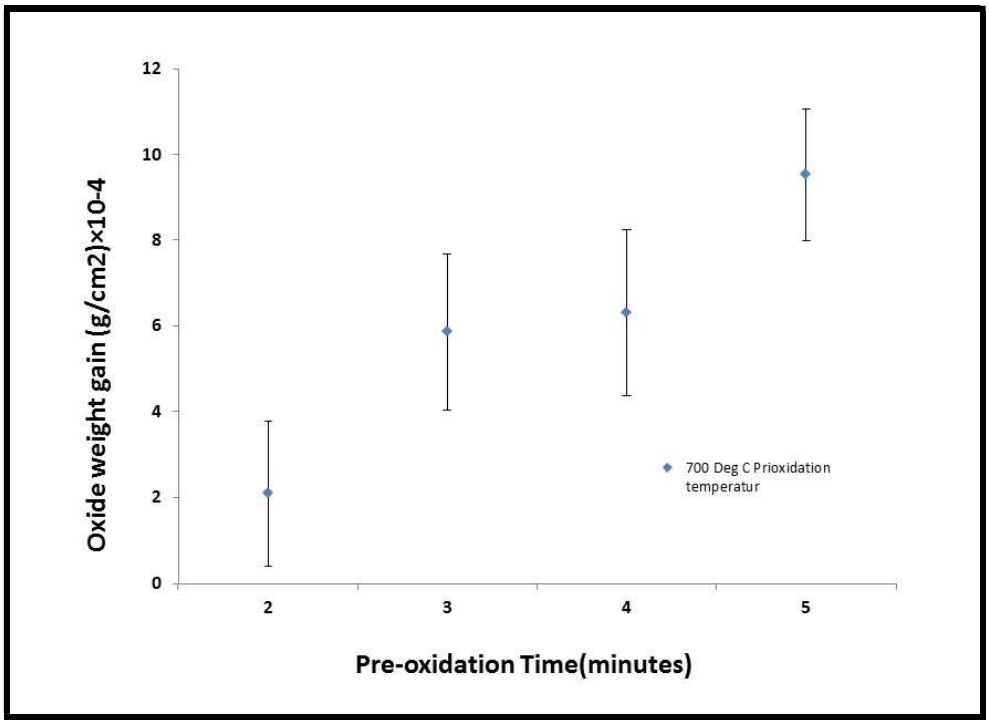


Figure 5.34: Oxide layer mass gain at different pre-oxidation temperature and at different pre-oxidation time

The optimum oxide layer mass gain (5.8666×10^{-04} g/cm^2) was achieved corresponding to pre-oxidation temperature at 700°C and the pre-oxidation time interval of 3 minutes. At this condition the maximum spreading (spreading area) of glass was observed. As pre-oxidation temperature increased above 700°C the surface degradation (flake surface) of the metal specimen was observed which reduces the wettability of glass over the metal substrate. The 700°C temperature was considered to be the most suitable pre-oxidation temperature where maximum wettability of glass with SS304 metal was observed and similar result were also reported for Kovar alloy.

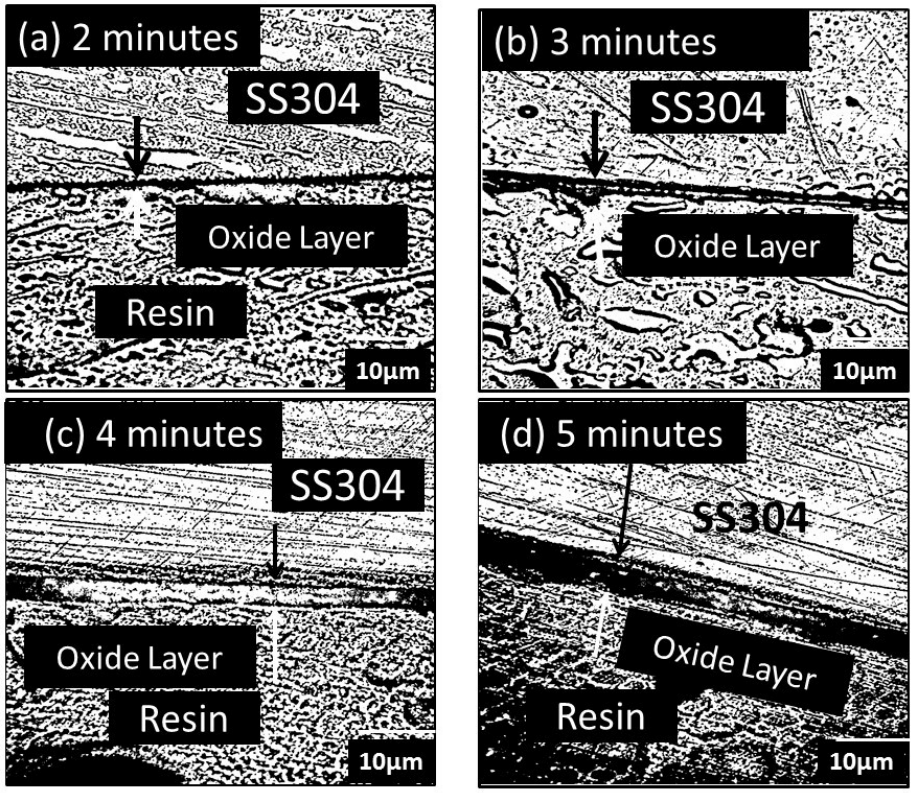


Figure 5.35: Oxide layer thicknesses (µm) at pre-oxidation temperature 700°C at different pre-oxidation time interval

Hence, further study was carried out for the measurement of oxide layer thickness at 700°C by varying pre-oxidation time (2, 3, 4 and 5 minutes) to obtain oxide layer thickness in range of (69.87-132.5 µm). The oxide layer thickness formed on the surface of the metal at 700°C, at different pre-oxidation time intervals of (2, 3, 4 and 5 minutes) was measured using an optical microscopy as shown in Figure 5.35 (a-d). The oxide layer thickness increased as pre-oxidation time increased as shown in Figure 5.35 (a-d).

5.6 TYPES OF OXIDE FORMED AFTER PRE-OXIDATION OF SS304 METAL SPECIMEN

The XRD analysis of SS304 alloy specimen in as received condition, pre-oxidation condition and at joining condition is shown in Figure 5.36. The as received SS304 metal specimen consists of chromium, iron, nickel and carbon phases. As metal is pre-oxidized at 700°C for 3 minutes, it was observed that FeO phase was formed in the alloy specimen as shown in Figure 5.36.
Luo and Shen also reported similar types of oxide formation for Kovar alloy after pre-oxidation. At pre-oxidation temperature of 700°C for 3 minutes, the Fe to O ratio from EDAX analyses was observed near to 1, as shown in Table 5.9. The Fe to O ratio confirms the presence of FeO (wustite) type of oxide phase having a closed cubic configuration, formed on the surface of metal specimen because of oxidation. The similar types of oxide were also observed in XRD analysis. The growth of FeO oxide phase on the metal surface takes place due to the decomposition of H_2O.

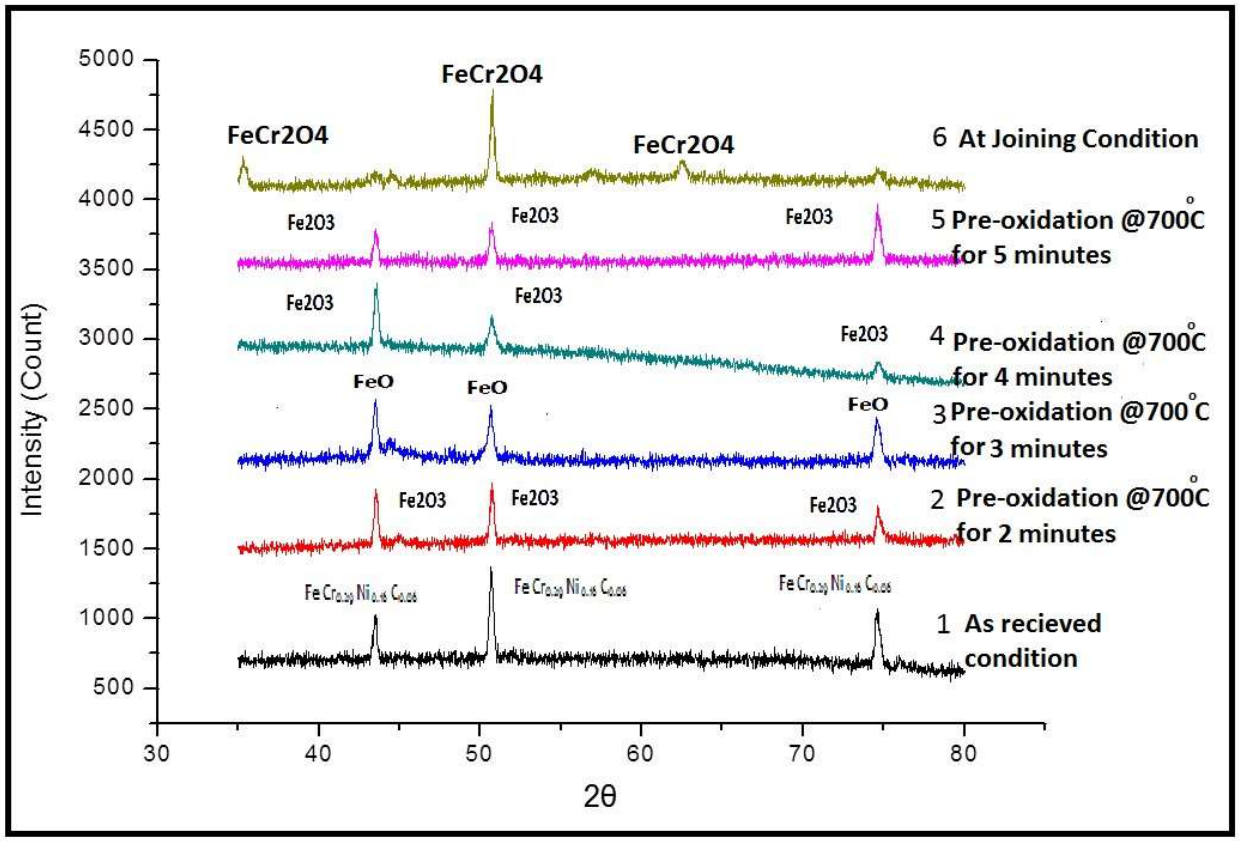


Figure 5.36: XRD pattern of SS304 metal substrate during, As-received, pre-oxidation with different pre-oxidation time and at joining condition

The dissociative oxygen gets transported to the metal interface and converts into oxygen ion. The Fe atom present in the metal specimen converts into ferrous ion and electrons which diffuse into the surface of the metal using reaction are given in equation:

$2\ H_2O(g) = 2\ H_2(g) + O_2$

$Fe^{2+} + O^{2-} = FeO$ ……(1)

The glass pallet during glass-metal joint fabrication process melts over the pre-oxidized metal specimen and reacts with (FeO) oxide phase on metal specimen and forms adhesion with glass. The rapid diffusion of Fe^{2+} which is a glass former and highly soluble leads to the formation of diffusion gradient which is responsible for the strong adhesion at the glass-metal joint interface At 700°C pre-oxidation temperature and corresponding to 2, 4 and 5 minutes pre-oxidation time the Fe_2O_3 oxide phase was observed. The FeO type of oxide was reported as the most suitable form of oxide for adhesion whereas use of Fe_2O_3 phase was not recommended because of its loose structure. At the joining temperature 980°C, $FeCr_2O_4$ phase dominates as observed in the XRD pattern as shown in Figure 5.36. The scanning electron microscope images of oxide layer deposited on the surface of metal substrate after pre-oxidation at 700°C for 3 minutes is as shown in Figure 5.37. The elemental compositions obtained with energy dispersive x ray spectroscopy measured for region marked 1 and 2 in Figure 5.37 is shown in Table 5.8 as spectrum 1 and spectrum 2.

The elemental compositions measured for marked region 1 show the percentage of Fe, Cr, Ni, Co, O which is nearly close to the elemental composition of SS 304 as shown in Table 5.8. which confirms the presence of SS 304 in the marked region 1. The region 2 shows the percentage of oxide scale where Fe to O ratio was observed near to 1.001 which confirms the presence of FeO phase at the oxide layer. The phase formed and elemental composition of the phase at the surface of metal after pre-oxidation of metal specimen is shown in Table 5.9. The elemental composition obtained with EDAX along with the oxide layer mass gain, oxide layer thickness, Fe to O ratio and oxide phase at the different pre-oxidation time is shown in Table 5.9.

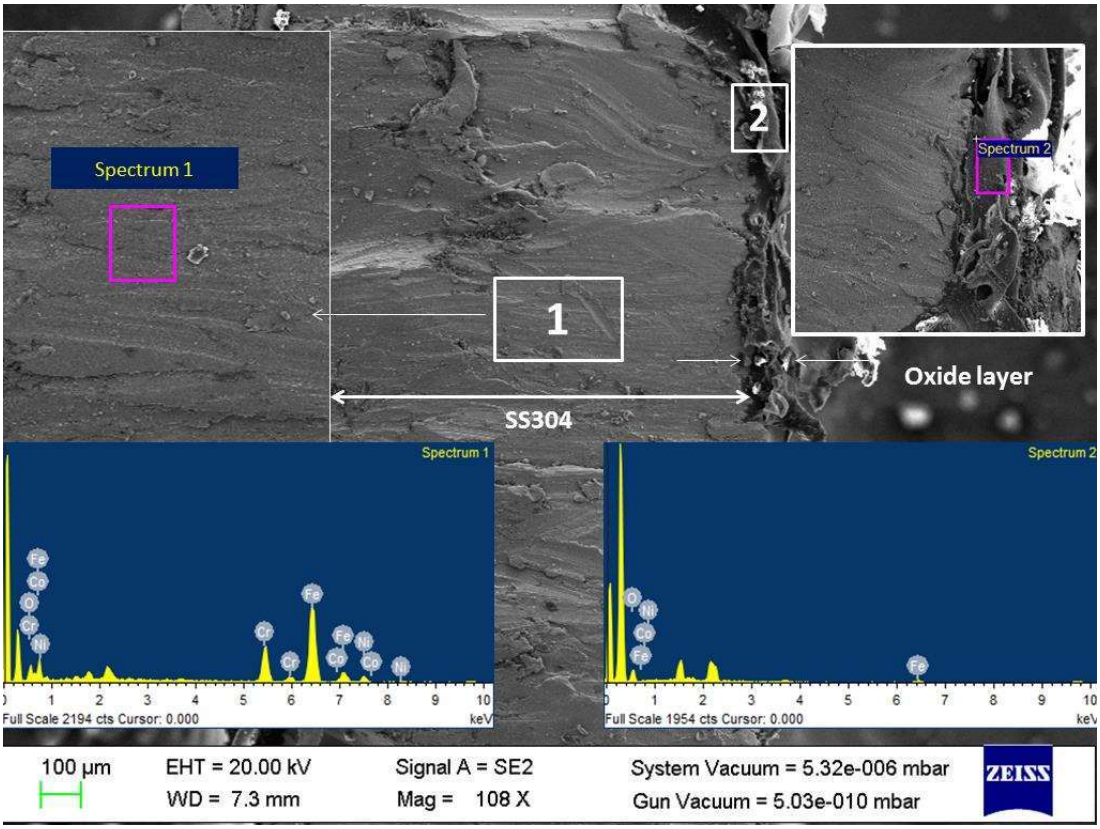


Figure 5.37: Oxide layer deposited on the SS304 metal specimen after pre-oxidation

Table 5.8 : EDAX elemental composition on SS304 specimen after pre-oxidation

	Weight %				
	Fe	Co	Ni	Cr	O
Spectrum 1	66.67	0.75	5.32	18.52	6.44
SS304	68	-	8	18-20	-
Spectrum 2	46.97	4.84	1.27	-	46.92

The identification of these phases was confirmed on the basis of Fe to O ratio obtained with energy dispersive x-ray spectroscopy as shown in Table 5.9 and XRD analysis as shown in Figure 5.36.

Table 5.9: Oxide layer mass gain and oxide layer thickness at different pre-oxidation time intervals

At 700°C pre-oxidation	Oxide layer mass gain(g/cm^2)	Oxide layer thickness(µm)	Elemental Composition				Fe/O Ratio	Oxide Phase
			Fe	Co	Ni	O		
2 minutes	2.09358×10^{-04}	69.87	35.87	3.74	4.65	55.74	0.64	Fe_2O_3
3 minutes	5.86667×10^{-04}	87.57	46.97	4.84	1.27	46.92	1.001	FeO
4 minutes	6.31795×10^{-04}	116.64	38.34	0.25	5.1	56.31	0.67	Fe_2O_3
5 minutes	9.54584×10^{-04}	132.95	36.56	2.47	6.1	54.87	0.66	Fe_2O_3

5.7 WETTABILITY AND ADHESION STRENGTH OF $40SiO_2$-$54B_2O_3$-$4Na_2O$-$2Al_2O_3$ GLASS SEALANT

The result of adhesion test between glass and metal interface has been studied along with wettability as shown in Figure 5.38. The mechanical load versus extension behavior under

applied tensile load was recorded using Universal Tensile Testing Machine as shown in Figure 5.38.

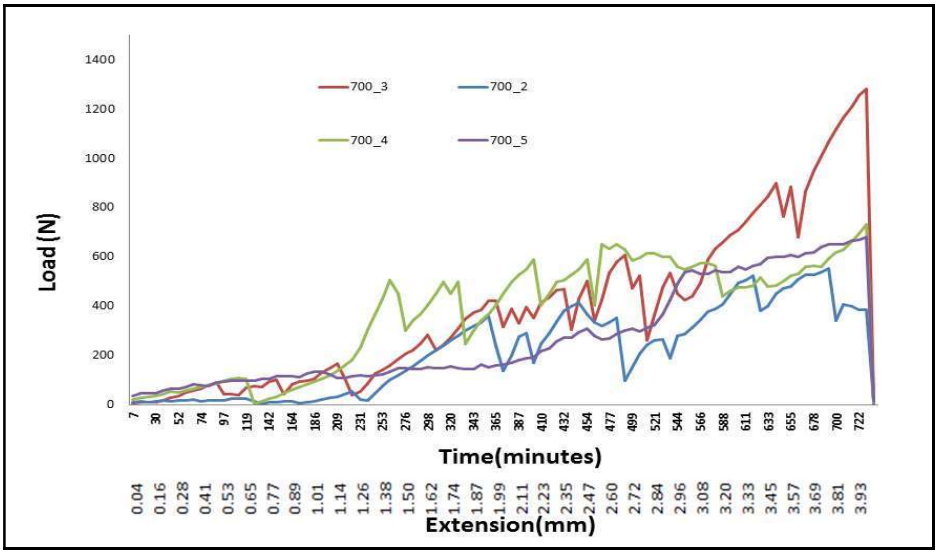


Figure 5.38: Load versus extension variation of glass-metal joint during adhesion test

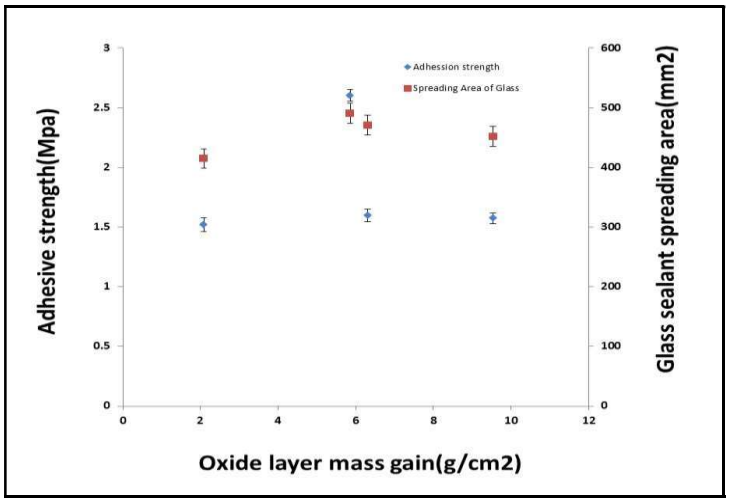


Figure 5.39 : Adhesion strength and spreading area of glass sealant with change in oxide layer mass gain

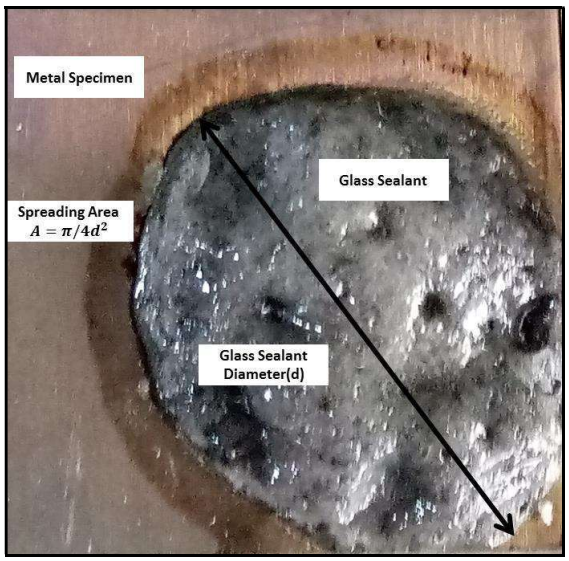


Figure 5.40: Estimation of spreading area of glass sealant over metal

The maximum tensile load bearing capacity was observed for specimen pre-oxidised at 700°C pre-oxidation temperature and for 3 minutes pre-oxidation time. The maximum load bearing capacity of the glass with metal ensured its maximum adhesion. The maximum spreading area of glass sealant pallet 490 mm^2 was observed corresponding to this condition as shown in Figure 5.39. The spreading area of glass sealant pallet was obtained from the visual examination as shown in Figure 5.40. The experimental result of spreading area and adhesion strength with change in oxide layer mass gain at 700°C pre-oxidation temperature for different time intervals is shown in Figure 5.39observed at 700 °C pre-oxidation temperature and pre-oxidation time of 2, 3, 4 and 5 minutes

5.8 INTERFACIAL STUDY RESULTS OF $40SIO_2$-$54B_2O_3$-$4NA_2O$-$2AL_2O_3$ GLASS SEALANT OVER SS304 METAL SPECIMEN

The types of phases present at the interface of glass-metal joint are shown in Figure 5.41. During the XRD analysis FeO, Al Na (SiO_4) and SiO_2 types of phases were present at glass- metal interface as shown in Figure 5.41. Similar types of oxides were also reported [Kaur.B et.al 2013].

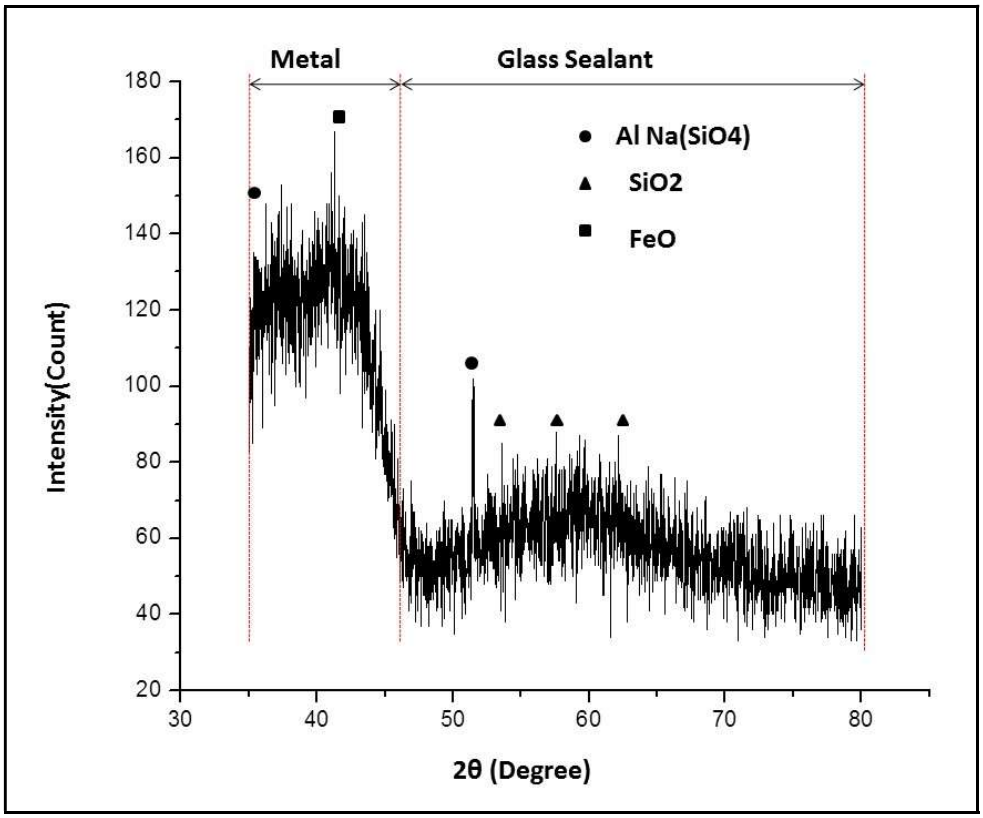


Figure 5.41: XRD pattern of glass-metal interface

The presence of FeO, Al Na (SiO_4) and SiO_2 types of phases at glass- metal interface confirmed the presence of both glass and metal as shown in Figure.5.41. The FeO phase confirms the metal oxide part whereas Al Na (SiO_4) and SiO_2 confirms the presence of glass phase containing Na_2O and Al_2O_3. The morphology of glass region at higher magnification 1000X on scale of 10µm is shown in Figure 5.42(b).

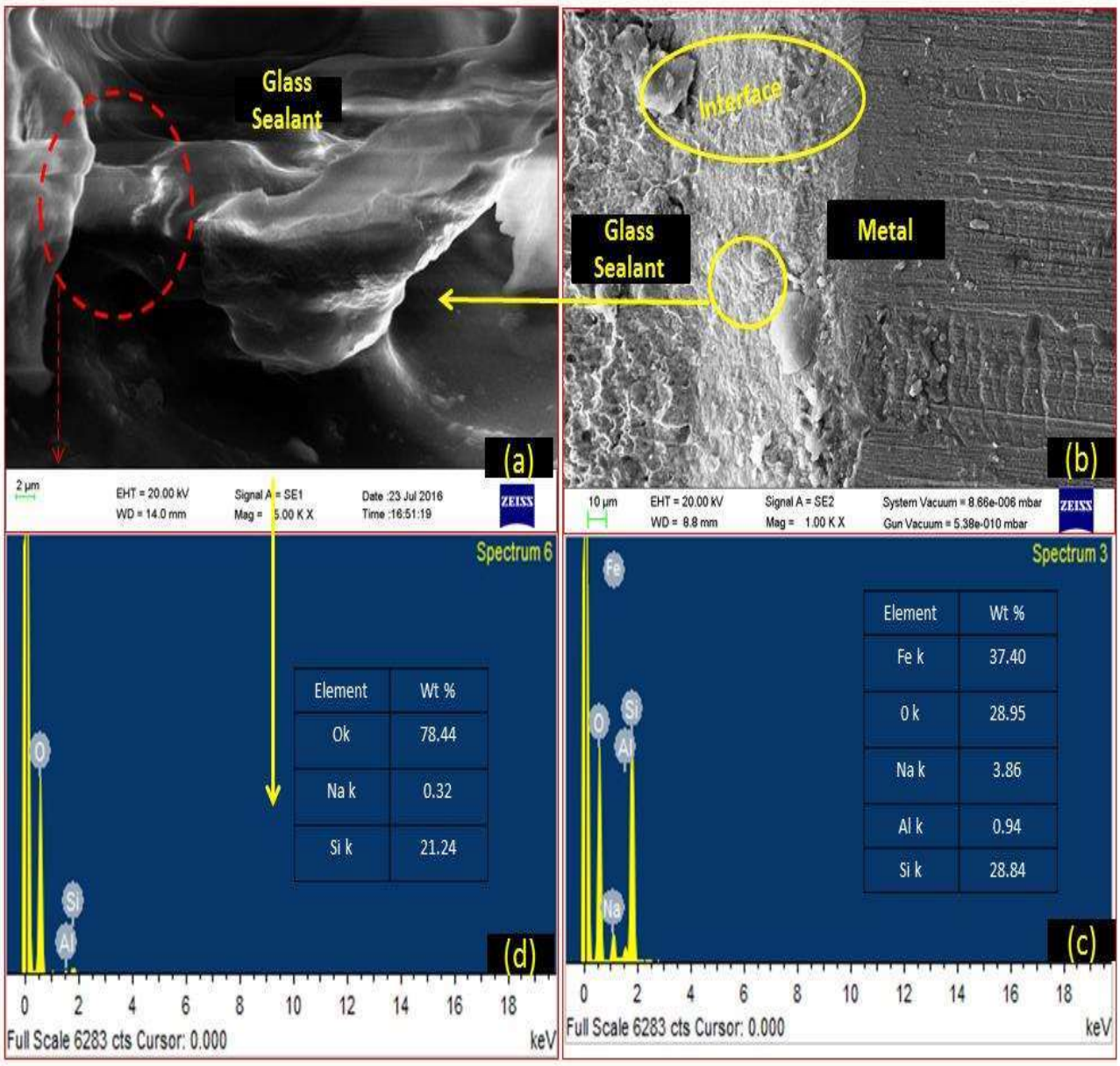


Figure 5.42: (a) SEM micrograph of glass sealant at 5 kx, (b) SEM micrograph of glass-metal joint interface at 1 Kx (c) EDAX image of glass-metal joint interface taken corresponding to 1 KX, (d) EDAX images of glass sealant taken corresponding to 5 KX.

The elemental composition obtained using EDAX (Energy Dispersive X-ray Spectroscopy) at the interface of glass-metal joint was obtained around Fe(37.40 wt%), O(28.96 wt%), Na(3.86 wt%), Al(0.99wt%) and Si(26.84 wt%). The distribution of Fe, Na, O, Si over the glass metal interface as shown in Figure 5.43 with X-ray dot mapping confirms the presence of these elements at interface.

The different colored dot describes the distribution of various elements on the interface region of the glass-metal joint. In order to see the morphology of glass-metal interface at higher magnification it was further observed under scanning electron microscope at magnification of 1000X on a scale of 10 µm as shown in Figure 5.42 (a). The EDAX of region marked at glass-metal interface was observed in as shown in Figure 5.42 (d). At glass sealant-metal interface marked in region Figure 5.42 (a) Fe, Si, Na, Al and O elements were present which confirm the presence of glass and metal along with oxides. The presence of glass was confirmed with the

presence of Si, O and Al at magnification of 5000X on scale of 2µm with the help of EDAX analysis as shown in Figure 5.42 (c).

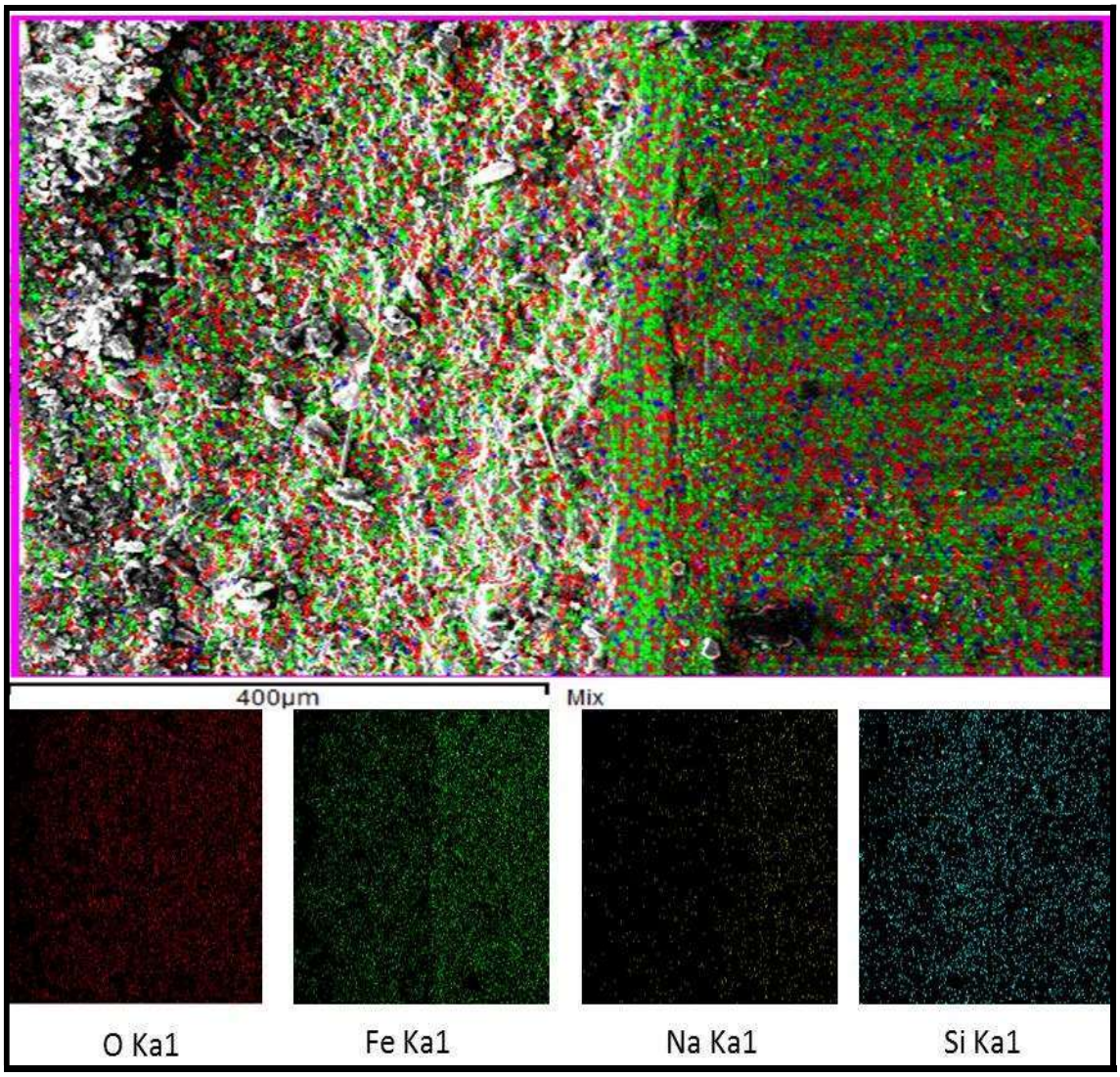


Figure 5.43: X-ray dot mapping at the interface of glass sealant-metal joint

5.9 VACUUM LEAK RATE IN GLASS-METAL JOINT

The vacuum in parabolic trough receiver tube is typically required to remain about 10^{-3} mbar with vacuum leak rate lower than 10^{-9} mbar l/s [13]. The loss of vacuum is responsible for the degradation of solar selective coating which may reduce the efficiency of parabolic trough receiver tube.

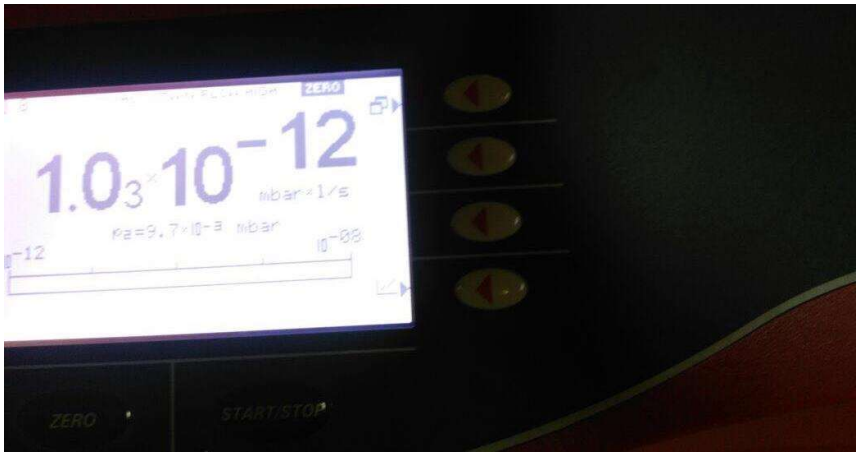


Figure 5.44: Level of vacuum leak rate achieved with leak testing

The level of vacuum leak rate obtained in compression glass-metal joint was observed to be 1×10^{-12} mbar l/s as shown in Figure 5.44.

5.10 IN-SITU WETTING BEHAVIOR OF $40SiO_2$-$54B_2O_3$-$4Na_2O$-$2Al_2O_3$ GLASS SEALANT OVER SS304 METAL SPECIMEN

The in-situ wetting behavior of glass sealant over SS304 metal substrate at different temperatures is shown in Figure 5.45 (a-i).

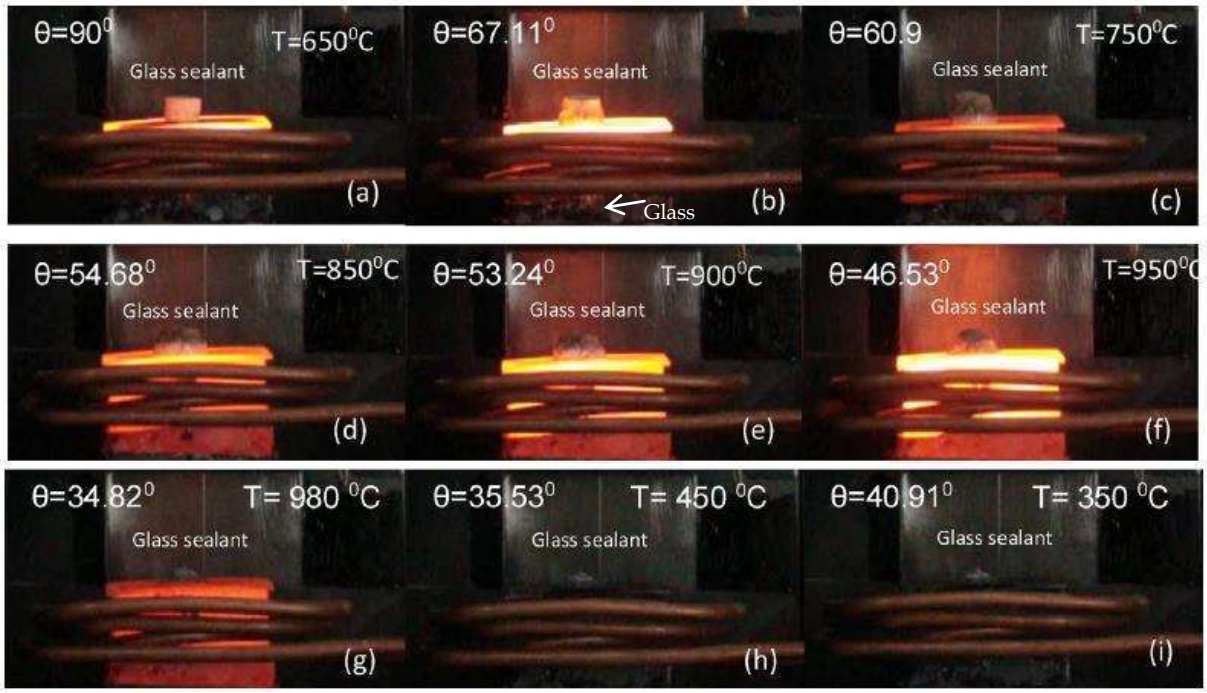


Figure 5.45(a-i) In-Situ wetting behavior of glass sealant over metal substrate at different temperature

The contact angle at different temperature was measured using "Digimizer" (Image analysis software). During the in-situ wettability analysis of glass sealant over the metal specimen, contact angle decreases with increasing temperature as shown in Figure 5.45 (a-g) and as glass cools from melting temperature to room temperature, contact angle starts increasing during cooling shown in Figure 5.45 (g-i).

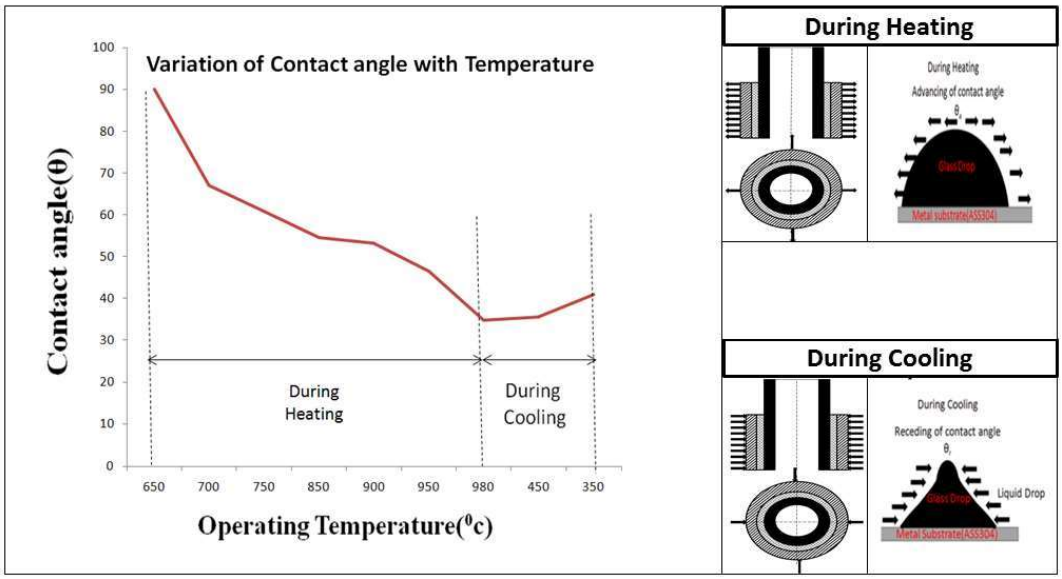
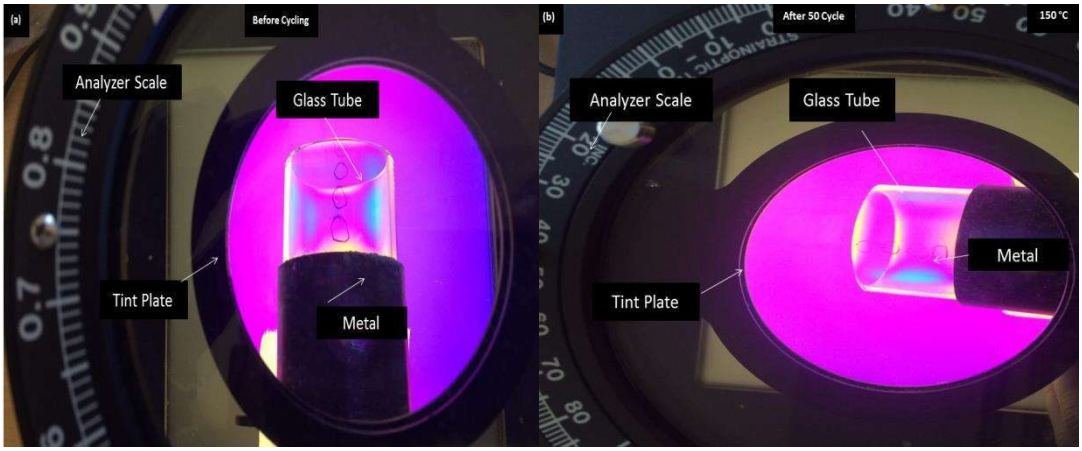


Figure 5.46: Variation of contact angle with temperature

The variation of contact angle of glass with respect to temperature is shown in Figure 5.46. The initial contact angle of glass sealant pallet measured was 90˚ and as the temperature increases the value of contact angle starts decreasing from 90˚ to 34.82˚ from room temperature to 980 °C. As glass sealant pallet cools from 980°C to 340°C the contact angle value starts increasing from 34.82˚ to 40.91˚. The increase in contact angle is due to the shrinking of the glass. During glass-metal joint fabrication as shown in Figure 5.46, it is observed that the glass expands during heating due to expansion of the metal ring in outward radial direction. Whereas as the assembly cools from 980 °C to room temperature the metal ring starts producing radial compressive force in glass sealant and glass tube, hence the contact angle of glass sealant pallet starts increasing which confirms that the glass sealant has been subjected to compressive loading during cooling. The resulting compressive force in the glass sealant and the glass tube allows the joint to resist high mechanical stresses.

5.11 STRUCTURAL INTEGRITY ASSESSMENT OF GLASS-METAL JOINT

The residual stress generated inside the glass tube was measured to be higher at 250 °C for 50 cycles as compare to 200 °C and 150 °C. The residual stress distribution in glass tube after 50 thermal cycles is shown in Figure 5.47(a-f). The condition of the glass-metal joint after the thermal cycling testing is as shown in Figure 5.49. The changes in the intensity of residual stress after thermal cycling at different temperatures are as shown in Figure 5.47 (a-f).



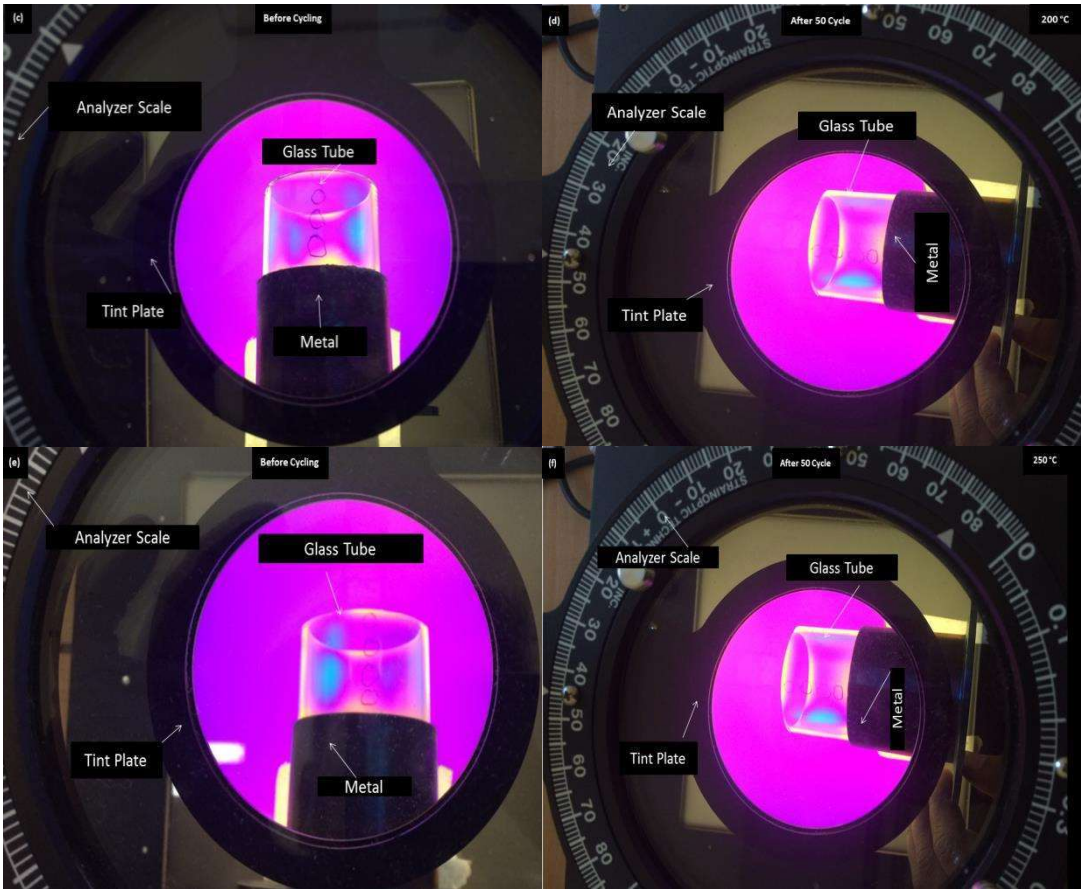


Figure 5.47 (a-f): Residual stress distribution glass-metal joint subjected to thermal cycling for different temperature 150 °C, 200 °C and 250 °C respectively

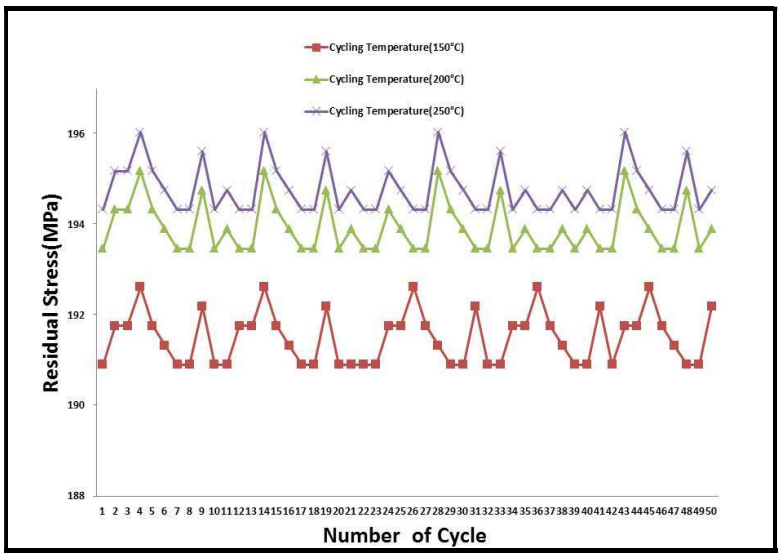


Figure 5.48: The residual stresses variation in compression glass-metal joint subjected to thermal cycling for different temperatures

The maximum residual stresses in the GMJ (Type1) were observed to be maximum corresponding to 250°C thermal cycling temperature as shown in Figure 5.48. The quality of glass tube in after the fabrication of GMJ was observed to be free from any crack even after the thermal cycling of 50 cycle at 250 °C in heating environment of oven.

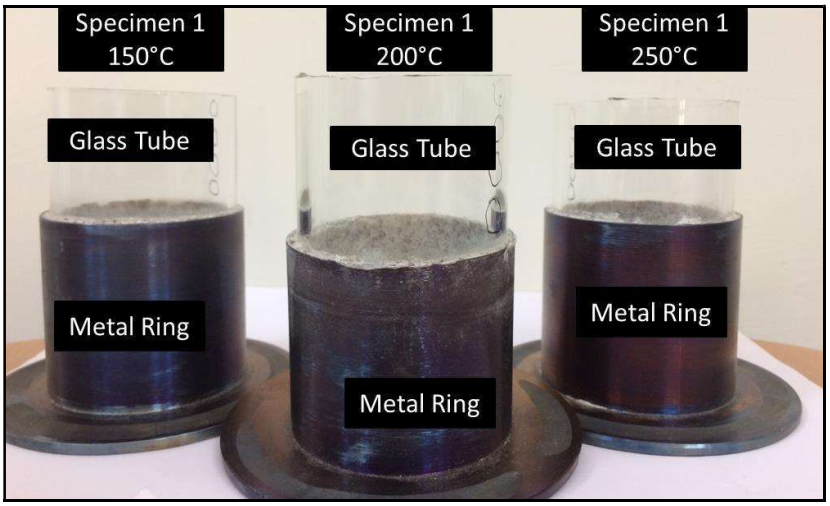


Figure 5.49: Compression glass-metal joint specimen for thermal cycling testing

The result obtained through the thermal cycling of glass-metal joint in environmental condition has shown the glass-metal joint was stable in environment after a time period of 200 hours. The as-received SS304 was stable in water and atmosphere condition over the exposure time of 200 hours as shown in Figure 5.50. The GMJ1 (Type2) specimen was found to be stable in the environment over the exposure time of 200 hours as shown in Figure 5.50. The macrograph of GMJ subjected to atmosphere are as shown in Figure 5.51 (a-h).

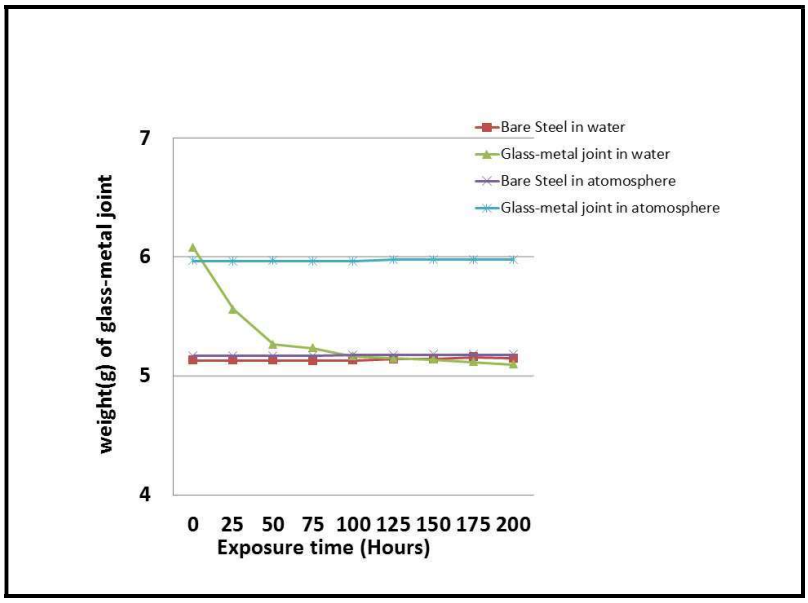


Figure 5.50: Change in weight of glass-metal joint specimen subjected to different cyclic loading

On the other hand the degradation of GMJ1 (Type2) in the water medium over a period of time was obtained faster as compare to GMJ2 (Type2) subjected to an atmospheric condition. The glass layer from the surface of the metal detaches up to 25 hours of immersion time in water solution as shown in Figure 5.52 (a).

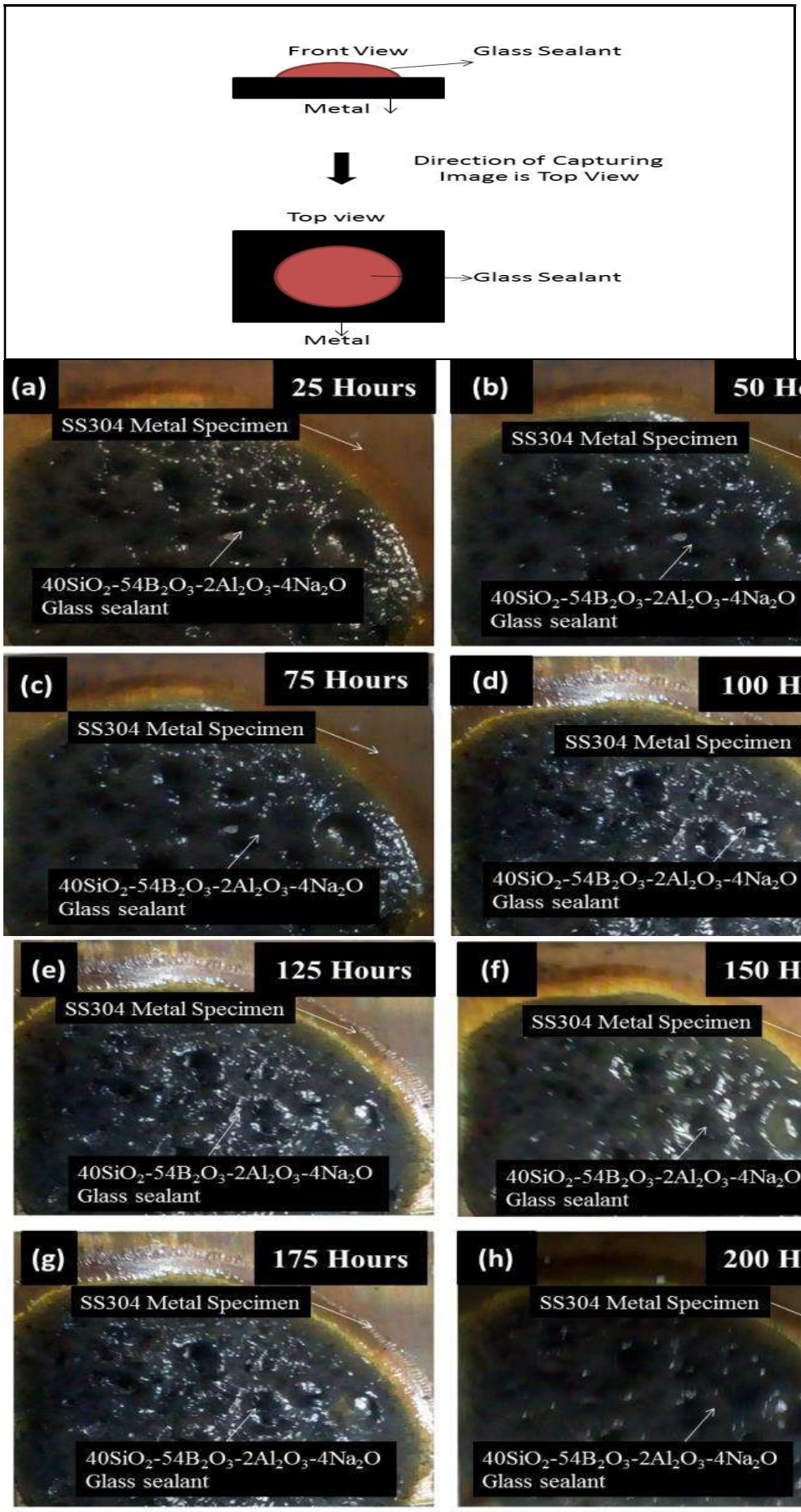


Figure 5.51 : (a-h) Macrograph of glass-metal joint after subjecting to atmospheric cycling for different time duration

The glass sealant from the surface of metal detaches completely after 50 hours of immersion time as shown in Figure5.52 (b). The phenomenon of GMJ degradation increased continuously at the GMJ interface with an increase in immersion time as shown in macrograph of the glass-metal joint as shown in Figure 5.52 (c-h). The degradation of glass sealant over metal SS304 metal specimen was observed because of the higher percentage of B_2O_3 in $40SiO_2$-$54B_2O_3$-$4Na_2O$-$2Al_2O_3$ glass sealant system. The higher percentage of B_2O_3 in glass sealant system reacts with water and forms boric acid which is readily dissolved in water [Shah.V et al., 2009].

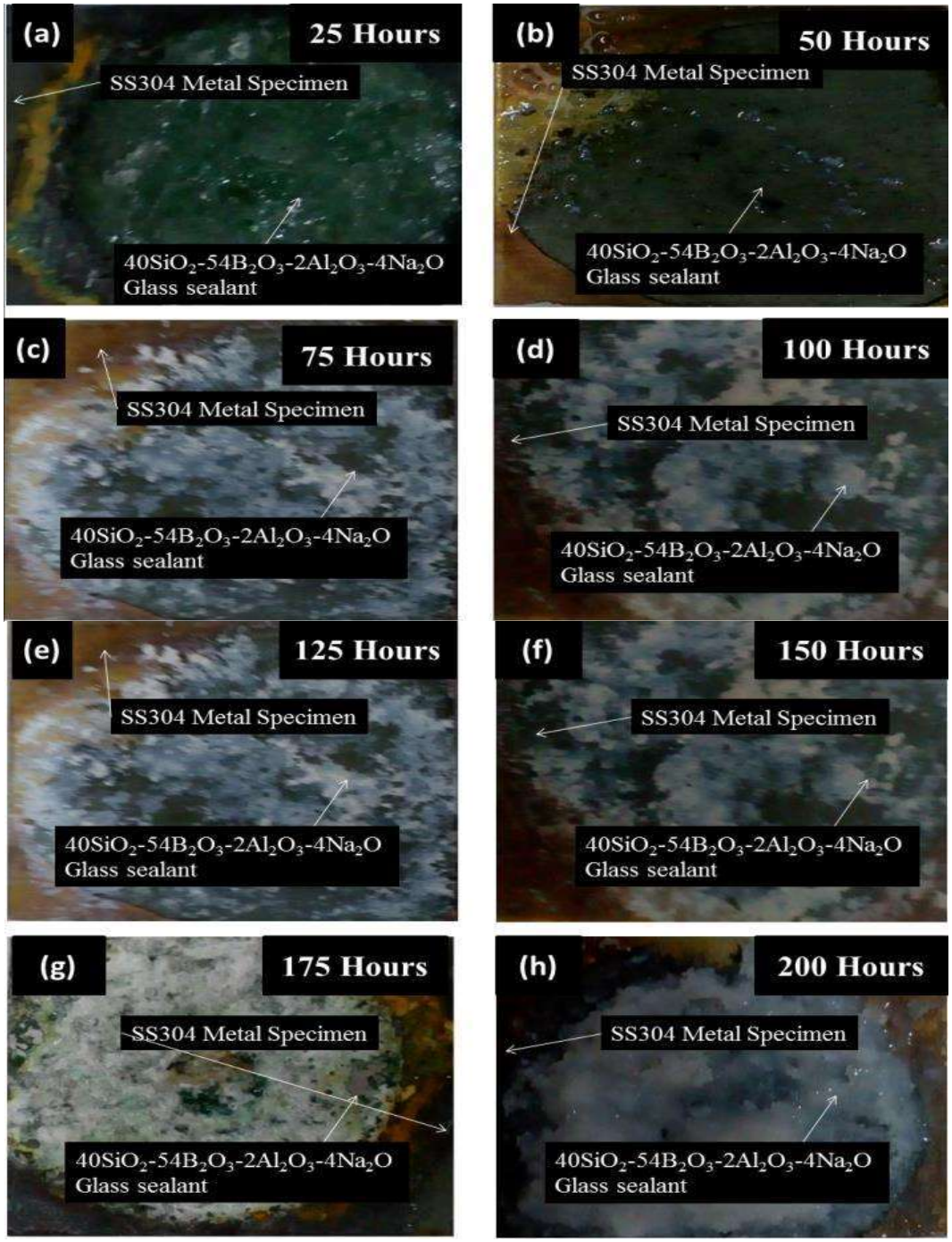


Figure 5.52(a-h): Macrograph of glass-metal joint after exposing to water environment cycling for different time duration

During the thermal cycling of GMJ3(Type2), GMJ4(Type2) and GMJ5(Type2) at 150,200 and 250°C both glass metal expands with different rate because of the difference in CTE. The difference in CTE of SS304 metal specimen and glass sealant during thermal cycling testing leads to the development of residual stresses at the interface. The thermal cyclic weaken the strength of joint. In present work glass sealant remained stuck with SS304 metal specimen even after the thermal cycling of 50 cycle at 250°C. The micrograph of the glass-metal joint after 50

thermal cycling in the muffle furnace is shown in Figure 5.53 (a-c). The glass sealant was remained stuck remain with metal even after the thermal cycling of 50 cycles at the different temperature. The change in weight of glass-metal joint specimen GMJ3 (Type2), GMJ4 (Type2) and GMJ5 (Type2) at different cycling temperature.

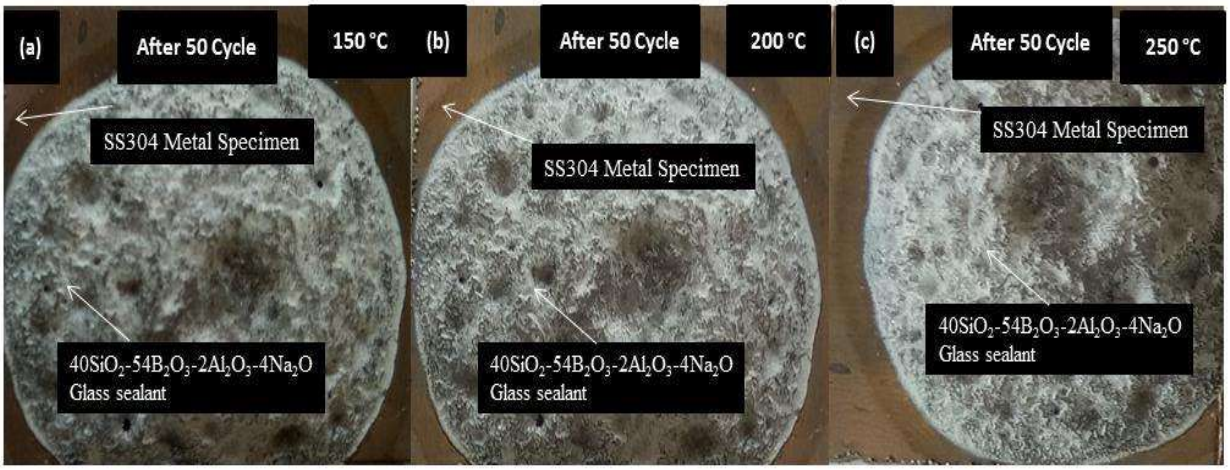


Figure 5.53: (a-c) Macrograph of glass-metal joint condition subjected to different cyclic loading temperature

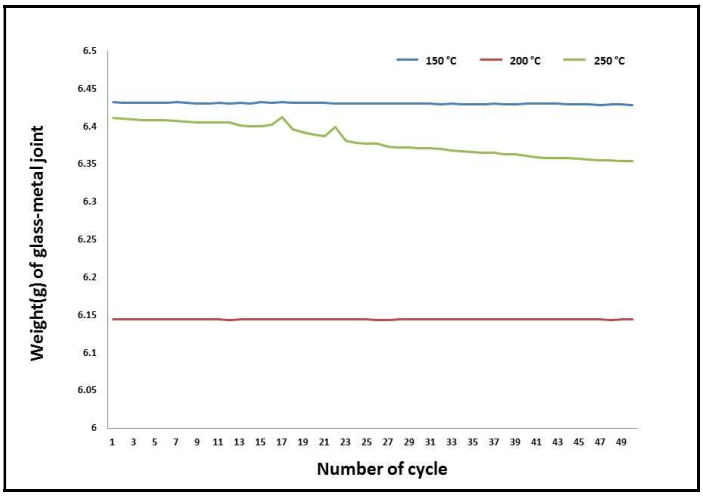


Figure 5.54: Change in weight of glass-metal joint specimen subjected to different cycling loading at different temperature

The change in weight of specimen was observed to be almost uniform in case of 150 °C and 200 °C whereas the change in weight of GMJ decreased in case of GMJ5 (Type 2) specimen at temperature of 250 °C as shown in Figure 5.54. The 250 °C is the maximum temperature where weight loss of the glass-metal joint started to decrease after the 5 cycle and it kept on decreasing as the number of cycles increased.

5.12 SUMMARY

The results of the experimental investigations such as surface roughness measurement, pre-oxidation study, Microstructural evaluation of the material for selecting the candidate material for investigation have been presented. The residual stress measurement in glass-metal joint and its relationship with metal thickness has been analysed. The effects of SiO_2 /B_2O_3 ratio on the thermal properties and structure of glass sealant has also been investigated. The wettability and adhesion strength of the suitable glass sealant has been investigated. The residual stress measurement was carried out for glass-metal exposed to thermal cycling. SS304 metal specimen was obtained as candidate material among copper and LCS 1018 metal specimen on the basis of

pre-oxidation, wettability, surface roughness, oxide phase and microstructural study. The 0.4 mm metal ring thickness was observed to be the adequate thickness on the basis of residual stress and thermal expansion mismatch measurement. BG6 glass sealant was obtained to be the suitable glass sealant which exhibit higher wettability, adhesion strength and lower Tg and Tc. 700°C peroxidation temperature for 3 minute pre-oxidation time was observed to optimum pre-oxidation condition where lower value of contact angle and higher adhesion strength was obtained because of the presence of FeO oxide phase. The interfacial study at the joint interface shows that the presence Fe, Na,O and Si over the interface confirms the presence of these element at the interface. 0.4 mm metal ring thickness taken as adequate thickness and glass-metal joint was scaled up from 29mm diameter to 62mm diameter and joint is then subjected to thermal cycling temperature of 150°C, 200°C and 250°C for 50 cycles. The intensity of residual stress was found to be the maximum in 250°C for 50 cycles. The glass-metal joint was stable in air as compare water medium for a time period of 200 hour.